FINITE-DIFFERENCE MODELING OF THE BATCH PROCESS SMOLDERING COMBUSTION OF WASTEWATER

A Thesis

presented to

the Faculty of California Polytechnic State University,

San Luis Obispo

In Partial Fulfillment

of the Requirements for the Degree

Master of Science in Mechanical Engineering

by

Laura Kawashiri

June 2018

COMMITTEE MEMBERSHIP

TITLE:	Finite-Difference Modeling of the Batch Process Smoldering Combustion of Wastewater
AUTHOR:	Laura Kawashiri
DATE SUBMITTED:	June 2018
COMMITTEE CHAIR:	Andrew Davol, Ph.D. Professor of Mechanical Engineering
COMMITTEE MEMBER:	Richard Emberley, Ph.D. Assistant Professor of Mechanical Engineering
COMMITTEE MEMBER:	Andrew Kean, Ph.D. Professor of Mechanical Engineering

ABSTRACT

Finite-Difference Modeling of the Batch Process Smoldering Combustion of Wastewater

Laura Kawashiri

A MATLAB model was developed for the smoldering combustion of wastewater in the context of a decentralized residential wastewater treatment appliance. Data from a batch process sewage smoldering experiment was simulated using implicit finite-difference approximations, assuming one-dimensional transient conductive heat transfer. The time-dependent temperature profiles within the column represented the main parameters of interest and were used to verify recoverable heat energy estimations. Given that the modeling method used for this thesis represents a unique approach, the assumptions and limitations of this model are thoroughly described in the context of reproducing results for other smoldering setups. A lack of convergence is seen in the model validation section of this report. Consequently, the practicality of this particular model contains significant limitations. Theoretical applications are also discussed and analyzed in terms of comparisons to modern alternatives and prototype feasibility.

Keywords: smoldering combustion, batch process, backwards difference

ACKNOWLEDGMENTS

Many thanks to my committee for their support and guidance. Thank you to Dr. Drew Davol for his wisdom and patience as my mentor, friend, and part-time therapist through this project. Thank you to Dr. Richard Emberley for providing the expertise that served as the technical foundation for my work and the logical checks for my sanity. Thank you to Professor Andrew Kean for agreeing to join my committee so last minute and offering his valuable constructive critiques. Thank you to Mr. Tod DuBois for introducing me to this project that has explored so many areas in which I was previously unfamiliar and uncertain. Thank you to the Cal Poly Mechanical Engineering Department faculty and staff for this incredible learning experience and the ability to further my education.

Thank you to my wonderful, wacky family for their endless support and constant encouragement. Thank you to my Uncle Seiki, whose kindness and generosity made my education possible. Thank you to my mom for every care package and card she sent telling me to "hang in there". Many times, those would be the highlight of my week. Thank you to my dad for always trusting me to figure things out even when I felt clueless. Thank you to my grandma for her cheerful spirit and reassurance. Thank you to my grandpa, whose career and obsession as a theoretical physicist first introduced me to science. Thank you to my second family for always showing their enthusiasm, loud and proud. Thank you to best friend and honorary sister for having my back since fifth grade and for knowing me better than I know myself.

Thank you to my amazing friends, all of whom lead their lives with so much passion, drive, and perseverance. I've been so fortunate to be surrounded by peers who inspire me with their own bright futures and ambitions. We worked hard, and we played hard. Thank you for filling my college years with adventure and laughter. Cheers!

TABLE OF CONTENTS

LIST OF TABLES

LIST OF FIGURES

NOMENCLATURE

A_c	=	Cross-sectional area of the waste column
α	=	Thermal diffusivity
Bi	=	Biot number
c_p	=	Specific heat capacity of the fuel matrix
ε	=	Emissivity
Fo	=	Fourier number
H_c	=	Heat of combustion for dry fuel
h_{eq}	=	Equivalent convective heat transfer coefficient (9 $\frac{W}{m^2K}$)
h_r	=	Radiation heat transfer coefficient
k	=	Thermal conductivity of the fuel matrix
$\dot{m}$	=	Mass rate of destruction for dry fuel
ρ	=	Density of the porous fuel matrix
σ	=	Stefan-Boltzman constant
T_f	=	Virgin fuel temperature (50 °C)
T_{ig}	=	Ignition temperature (250 °C)
T_s	=	Surface temperature
T_∞	=	Surrounding air temperature (25 °C)
Δt	=	Time step
Δx	=	Mesh size

Chapter 1

INTRODUCTION

Biological waste will always exist as one of the many byproducts of human activity. Any facility that hopes to provide an acceptable standard of living requires some process for properly evacuating and treating human waste. As society continues to grow and advance, so too will the amount of raw sewage. Consequently, both developing and developed countries will face challenges regarding the collection and treatment of their waste. While the majority of sanitation projects address the issue of providing reliable facilities to developing communities, few have offered more efficient alternatives to modern sewage treatment systems. Despite the long history of functional success demonstrated by centralized plumbing in developed areas, its inherent challenges and high water demand prompt many to question the sustainability of such methods.

Characterized by a standard flush toilet connected to a communal main sewer line, centralized systems feature numerous inefficiencies due to their subterranean complexity and high servicing volume. The nature of distributed underground sewage pipes entails major difficulties regarding installation, maintenance, and flexibility. Such networks can require extensive excavation projects and hundreds of hours of labor to complete, which accounts for significant expenses in new home construction. For a single family home, the national average for a sewer main installation alone stands at $2,500 to $2,900, not including connection fees and utilities [8] [23]. The cost range, however, can extend from $1,000 in well-established urban areas to $40,000 for those living in remote locations or on complex terrain [21]. Because the main structures reside underground with minimal access points, maintenance and repairs can result in an equally expensive bills, as replacing damaged or deteriorating piping

demands similar excavation procedures. In addition, performing sewer maintenance often results in inconvenient situations for entire neighborhoods due to road closures and temporary water shut-offs. As a result of high installation and maintenance costs, minimal design flexibility, and lengthy construction times, centralized systems also struggle to serve rapidly urbanizing communities. While modern society has enjoyed the benefits of communal sewers, the challenges that accompany large underground piping networks provide plenty of motivation for researching simpler alternatives, even before considering their resource inefficiencies.

Traditional sewers provide the convenience of avoiding direct responsibility for individual sewage treatment. This luxury, however, requires significant amounts of water for waste collection and transportation. The United Nations 2017 World Water Report estimates the global demand for water to rise 50% by 2030. Statistics such as this raises concerns, especially in drought-affected areas like central California, where water conservation has become a pressing issue. The city of San Luis Obispo reported in 2016 that 41% of their water demand came from single-family homes and 22% from multifamily homes, making residential units responsible for 63% of the water demand [12]. With current estimates that toilet flushing uses 31% of household water, this presents a major area for reducing consumption on both a residential and city-wide scale [28]. In addition, outside of San Luis Obispo, effluents of varying quality, from rainwater to industrial waste, become funneled together while travelling through the sewers. On their own, rainwater and other less hazardous flows require less rigorous treatment and can contribute to grey water reservoirs before entering the waste stream. Current practice, however, produces a massive, diluted waste volume, which requires more energy to pump and process.

In response to high installation costs and trends toward more sustainable options, families seeking to build new homes or remodel existing systems have gained interest in alternative waste disposal methods. Sangha Energy, a Northern California

company specializing in distributed power, water, and waste, has requested assistance researching on-site wastewater treatment alternatives to implement in off-grid residences. After studying various methods and prototypes for off-grid sanitation solutions, smoldering combustion surfaced as a recently-introduced waste treatment option. While smoldering phenomena has been studied for years in the context of fire safety, its potential in the sanitation industry has only been introduced in the last decade. Although sewage smoldering has produced promising experimental results in other studies, further research towards understanding the heat transfer behind it in a mathematical sense has yet to be published.

1.1 Objective

At the core of this project, the desired outcome was to develop a simplified model for smoldering combustion specific to residential sewage treatment. Although existing smoldering models account for factors such as micro-scale fluid dynamics, the higher-level math that accompanies these factors can present a difficult and possibly unnecessary obstacle if the effects are only minor. As a result, the mathematical characterization and computational modeling of the smoldering combustion of residential black water constituted the bulk of this thesis. Because of the pioneering nature of the methods under study, the modeling for this particular case of smoldering followed a sort of "bare-minimum" approach, where the experimental configuration was reduced to a highly-simplified form using basic assumptions. While expecting this approach to produce over-simplified results, the model would still provide some baseline for comparison with the published experimental data.

This project caters towards the parameters associated with a specific prototype system design with the idea that these parameters can later be manipulated to describe different configurations. The results of all subsequent analyses are, therefore,

represented in terms of the set up that was unique to the experiment that produced the data for correlation. In the best-case scenario, a fully-functioning model would be able to predict thermal behavior for energy recovery analysis, as well as comparison with alternatives. This information may later be used to suggest a more economical and sustainable solution to centralized wastewater collection and treatment.

The structure of this thesis paper has been organized as follows: Chapter 2 provides background information on various forms of modern sewage treatment, as well as the two state-of-the-art methods of interest. Chapter 3 covers the derivation of the governing equations and model development. Chapter 4 reveals and discusses the simulation results. Chapter 5 delves into the model validation through a convergence study. Chapter 6 explores the strengths, limitations and requirements associated with future development, as well as potential applications and concluding thoughts on the project.

Chapter 2

BACKGROUND

The following chapter introduces background information on the various circumstances and existing practices that have framed the context of this thesis.

The United Nations hierarchy of waste management methods includes prevention, minimization, reuse, recycling, energy recovery, and disposal, in order from most to least preferred. Because the prevalence of raw sewage will always accompany society, the best case scenario begins at minimization, with most American homes operating more often at disposal and sometimes energy recovery. Decentralized on-site options, however, offer methods for improved treatment along multiple points in this list. By reducing the scale to single residences, water consumption for transport and processing becomes negligible, minimizing the load volume in need of treatment. In minimizing its dilution, reuse, recycling, and energy recovery from wastewater can occur with greater ease. In nature, feces represents a vital component of the environments nutrient cycle as a condensed form of nitrogen, phosphorous, potassium, and organic matter. After pathogen removal, such components may be extracted and reused as fertilizer and the water from dehydration recycled as either grey or, in some cases, potable water. In addition, numerous energy recovery techniques accept sewage-derived organic compounds as fuel and can exhibit potential for operating at a residential scale. The performance of such energy recovery mechanisms constitutes a major application goal for this thesis.

Prior to discussing the various methods for treatment and energy recovery, a few key terms must be defined. Innovations in waste treatment often mention pyrolysis, combustion, incineration, and gasification, yet not all explain the differences and relationships between them explicitly. Pyrolysis is defined as the heat-induced chemical

decomposition of organic matter with negligible or zero oxygen presence. This process yields carbon-based gases and solid carbon residue or char, with the remaining components condensing to form a viscous liquid byproduct known as pyrolytic oil or bio-oil. Combustion describes the chemical reaction characterized by the addition of oxygen and the production of heat and light as a flame. A fuel undergoing combustion first endures the process of pyrolysis, succeeded by the input of oxygen, which reacts with the resulting char and carbon gases. Complete combustion of carbon-based fuels typically emits gases such as carbon dioxide, carbon monoxide, and water vapor. Incineration refers specifically to the treatment and disposal method that performs combustion at high temperatures using large volumes of air. Incineration plants may then use the heat produced to run steam turbine generators to generate electricity. The toxicity of its ash and volatile derivatives, however, have earned this solution much criticism regarding environmental and health hazards. The final term, gasification, offers an alternative to combustion as a process that converts organic waste into synthetic gas, or Syngas, using high temperature, high pressure, and minimal oxygen. The restricted oxygen input distinguishes this method from combustion as more of an extended pyrolysis technique that maximizes the production of volatile carbons. These gases may then be harvested as Syngas and further refined into high-value fuels, chemicals, and fertilizers. Like pyrolysis, residuals include char and pyrolysis oil, which can combine to form a slag [4] [24] [26]. All four terms have a major presence at the forefront of the waste management industry, where sanitation innovators continue to explore a variety of more economical and sustainable solutions to a problem that has attracted some of the worlds most influential organizations.

In 2012, the Bill Gates Foundation launched the Reinvent the Toilet challenge, where university teams designed prototype toilet units for residents in developing nations. These semi-portable, self-contained units serve up to 10 people, cost less than five cents per day to operate, consume no water, harvest energy from fecal

waste, and produce either inert or reusable byproducts. Two of the entries that appeared relevant to this thesis included the Cranfield Nano Membrane Toilet and the Smoldering Toilet from the University of Toronto [17] [27]. Studying these examples has offered a small glimpse into the future of wastewater treatment technology, and, although waste-biomass gasification has been practiced since the early 20th century, experimental sewage smoldering has only appeared in literature within the last fifteen years. As a result, this method presents an exciting frontier for exploration.

2.1 Modern Practices for Residential Wastewater Collection and Treatment

Before delving into the most recent advancements, it is useful to review the current waste treatment practices that have shaped the sanitation environment. This section discusses centralized sewage systems and treatment plants, as well as septic tanks, in further detail, given that they constitute the two most prevalent residential wastewater treatment systems. Alternative decentralized setups such as portable toilets, composting toilets, anaerobic digestion reactors, and constructed wetlands also receive mention as functioning, but less common solutions.

2.1.1 Centralized Sewage Systems

In terms of cultural acceptance, the standard flush toilet represents the universal symbol for proper human waste treatment. This familiar option demonstrates the prevalence of centralized sewage systems within developed communities. Although a wide variety of treatment processes exist and are compatible with centralized systems, the majority follow the same basic flow illustrated in Figure 2.1. Residential units flush out raw sewage from individual toilets into communal subterranean sewer lines, where the waste collects and flows to a distant treatment plant in large volumes on

the order of millions of gallons per day. Upon arrival at the plant, the untreated domestic wastewater, or influent, undergoes primary treatment, which acts as the first round of solid-liquid separation. A common practice within primary treatment is to include a preliminary treatment component. This step physically filters out larger solid obstructions by way of screens, filters, or other mechanical devices, so as to reduce the sludge contamination in the following operations. In the main process of primary treatment, the influent collects in a large basin where a lack of disturbance allows the solids to settle on the bottom while the fats, oils, and greases float and collect at the top to create a floc. Once these zones of sedimentation and flocculation have been established, the middle layer of supernatant liquid, now considered primary effluent, is extracted and pumped to a secondary treatment structure.

The majority of wastewater pathogen removal and disinfection occurs during secondary treatment. Here, various microbes consume the bio-hazardous nutrients, which are measured as biological oxygen demand, BOD, based on the amount of oxygen required by the bacteria to metabolized the substrate [5]. Typically, the primary influent empties into a series of biological treatment basins containing the appropriate treatment bacteria. The biochemical reactions take place over the course of a pre-designed hydraulic residence time, during which the nutrients are drawn from the fluid and used to synthesize new bacterial cells, which either coagulate into large clumps and sink or remain suspended in the liquid. The biodegradable nutrients plus the non-coagulated bacterial cells and residual minerals make up the value for total suspended solids, TSS. By means of a secondary settling tank, the treated water is then isolated and pumped out as secondary effluent. Often times, facilities featuring up to secondary level processing provide adequate wastewater treatment for environmental discharge. The quality of the secondary effluent discharge, however, must meet the district regulatory limits for both BOD and TSS, as well as other hazardous chemicals. At many plants, disinfection in the secondary stage is usually performed

by injecting chlorine into the secondary effluent. The negative environmental effects of chlorine, however, encourage zero tolerance for its presence in treatment plant discharge. This, then, requires the implementation of a tertiary treatment process, which consists of additional treatment steps that can include dechlorination and other processes to help facilities meet their discharge limits.

At most treatment plants, activated sludge systems constitute the standard method of handling the residual solid waste. The settled solids from both the primary and secondary treatment is pumped out and collected as the activated sludge, which contains the denser sewage particulates as well as dead treatment bacteria. The resulting sludge can, then, flow one of two ways: Recycle or waste. Recycled activated sludge gets pumped back into the influent flow to maintain microbial ecology within the treatment tank, while wasted sludge gets pumped away either to be dumped or treated with a digester. Subjecting the sludge to anaerobic digestion produces useful by-products, such as methane and fertilizer, which can then be sold as a source of revenue.

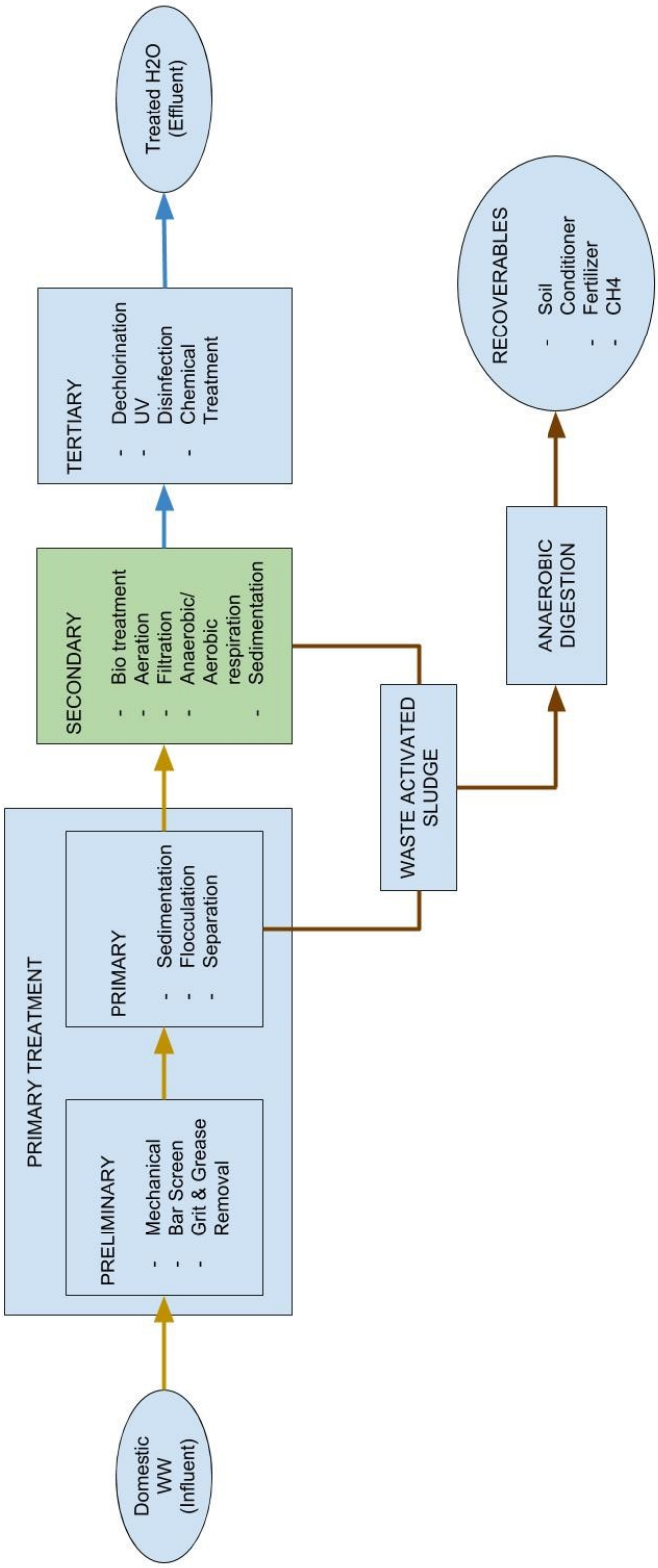

Figure 2.1: Basic wastewater treatment flowchart.

In terms of user experience, flush toilets and centralized systems provide the most hands-off approach to managing sewage. The lack of involvement in the treatment process appeals highly to most people and the convenience of such a system allows for an increasingly productive society. In addition, all the unpleasant aspects of waste treatment, including odors and pathogens, can be removed from their origin and handled in a more remote location, such that the average person can forget about their waste as soon as it is flushed. While nearly everyone has experienced at least one plumbing issue, the consensus remains that, overall, flush toilets and centralized sewers have consistently served as a robust and reliable waste removal system for developed communities.

While flush toilets may offer the ultimate convenience for users in more populated areas, the essentials for proper installation and maintenance can present their own obstacles, many of which may be worth avoiding all together. The practicality of standard centralized systems still remains dictated by the residence location. For those building homes near protected lands, far-removed from existing sewer mains, on mountainous terrain, or in extreme climates, centralized plumbing can become a much more stressful and expensive option than for the average homeowner. Piping installations require tons of excavation and hours of labor even in a standard setting, and the cost only increases when factoring in inclined surfaces or more challenging environments. The popular desire to build in scenic locations, however, maintains the demand for wastewater solutions in such areas. As a result, a variety of decentralized sewage treatment options exist for these more limiting situations.

2.1.2 Septic Tank Systems and Other Decentralized Alternatives

The most typical modern solution for off-grid residential sewage treatment is represented by septic tank systems. Instead of installing a main connection to a communal

sewer line, the main line from the house leads directly to a septic tank where primary treatment occurs via settling and flocculation. As shown in Figure 2.2, the mid-layer primary effluent then leaches into a drain field, where gravel, the underlying soil, and naturally occurring microbes provide the necessary secondary treatment before reaching the groundwater. With this method, the user avoids the cost of construction to connect to a central sewer main, while also benefiting from the familiarity of a typical flush toilet. At a national average of $5,400 with a higher limit of $15,000 for full system installation, septic tanks offer a more affordable alternative to a sewer main installation, which alone can cost upwards of $15,000 in similar locations [7] [8] [23].

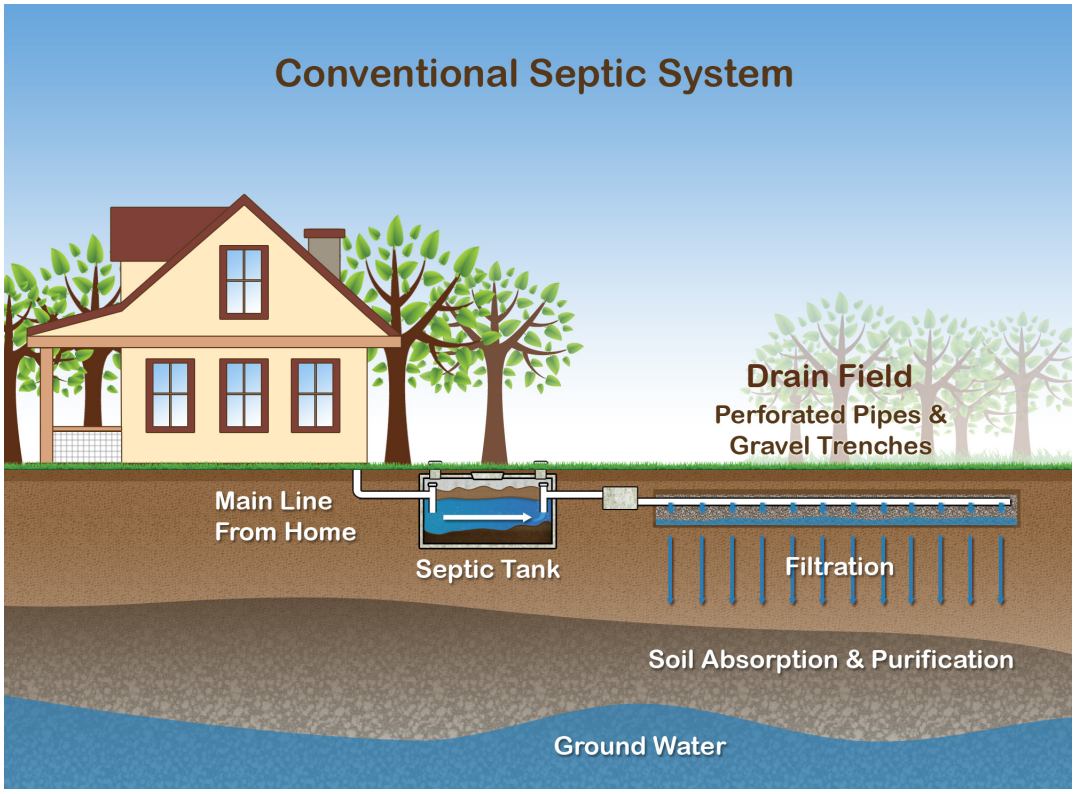

Figure 2.2: Schematic of a standard residential septic system. (Source: Skip Wooten Septic)

Although septic systems have been considered a next best compromise to centralized plumbing, the inherent maintenance processes can still present some inconveniences. The sludge that accumulates at the bottom of the tank must be pumped out

every three to five years and costs a few hundred dollars each time [34]. In addition, the feasibility of a septic system is determined greatly by the size, topography, and drainage quality of the surrounding land. Improper conditions can result in serious public health and environmental hazards should the drain field fail and result in untreated effluent contaminating groundwater or draining into surface waters. Septic tanks, therefore, while presenting a reasonably successful decentralized option, are not appropriate for every off-grid application.

Apart from septic systems, numerous other decentralized alternatives exist for waste processing with varying levels of treatment. The pros and cons of each, however, still result in the lack of a practical, permanent off-the-grid sewage solution for particular circumstances. Portable toilets, while used widely at construction sites and temporary outdoor venues, only function as sewage collectors and temporary containers without providing any form of treatment. As a result, poor sanitary conditions and odors make for a rather uncomfortable user experience and the contents must eventually be pumped out and treated at an appropriate facility. A step above that, composting toilets can provide the similar convenience of being a compact, self-contained unit while also offering treatment via natural decomposition. Proper maintenance, however, can be time-consuming and more involved than most people prefer and is necessary to prevent odors.

(a) Composting Toilet

(Source: Nature's Head)

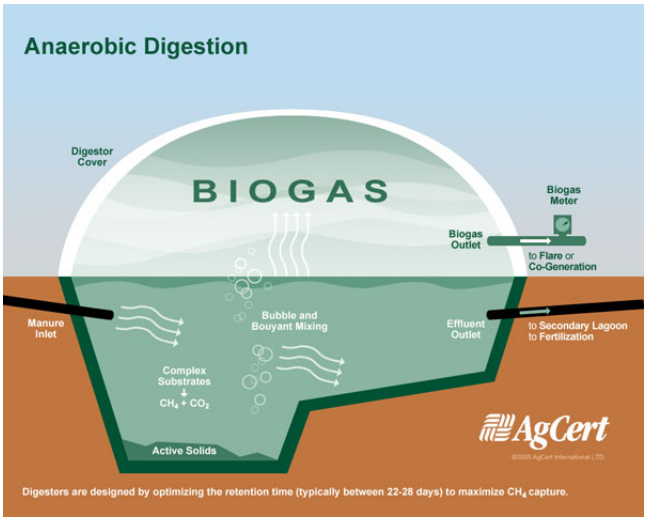

(b) Anaerobic digestion reactor

(Source: AgCert)

Figure 2.3: Decentralized sewage treatment alternatives.

Anaerobic digestion reactors have gained popularity in farming communities which handle large volumes of livestock manure [33]. Undergoing the same biological processes as the activated sludge in centralized systems, anaerobic digestion reactors degrade raw sewage to produce biogas and treated sludge to be used as fertilizer and soil conditioner. Although this encourages a more circular chain of resources, the practicality of this system becomes limited outside of a farm setting since the average residential home has minimal capacity to manage the complex micro-biome within a reactor. In addition, a lack of demand for the resulting fertilizer sludge would require extra dumping or removal action.

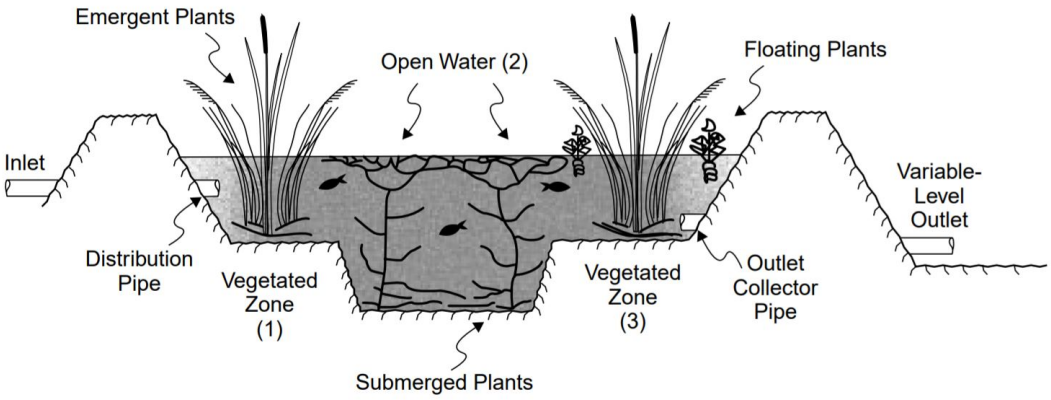

Figure 2.4: Schematic of a constructed wetland. (Source: EPA)

Constructed wetlands, which have gained popularity as part of the shift towards more sustainable building design, offer a multi-purpose, aesthetically pleasing solution for secondary and tertiary wastewater treatment. Both these and anaerobic digesters, however, still require large plots of land to support and major excavation to install. In addition, both still channel the final effluent in larger volumes to be drained in the ground. Much like septic tank systems, ground that naturally features poor drainage properties would inhibit successful operation of such a system. Because of these limitations, innovators have sought to avoid systems involving large outdoor structures by moving towards self-contained appliances instead. A more recent example on the market is the Incinolet, which incinerates raw human waste with a heating coil on a per use basis. The process results in a small amount of ash that the user empties weekly. Although the semi-portable, self-contained design of this appliance offers a major convenience and cost saving for the homeowner with respect to installation, the utility costs of powering the heating element are comparable to a clothes dryer for each use. Consequently, these units are not advertised as being compatible with solar systems, like many other appliances with large heating elements [9]. This device also lacks the ability to recover and reuse heat energy from the incineration pro-

cess. Recoverable energy, therefore, presents a niche that many new waste treatment appliance designs are trying to address.

The prototype designs studied in this thesis provide two examples of self-contained waste treatment appliances that employ heat treatment and energy recovery to create a self-sustaining system. The first Gates Challenge submission to be discussed is the Cranfield Nano-Membrane Toilet, which treats with gasification, a process that is explained further in the following section.

2.2 Wastewater Treatment via Gasification

In the last decade, the practice of solid waste gasification has gained interest due to the valuable by-products, as well as the relatively low environmental hazards associated with the process. This non-combustion alternative to incineration applies extremely high temperature and pressure to an oxygen-deprived environment, such that the feed degrades into mostly volatile molecules with proportionally small amounts of slag [18]. Beginning with coal in the Industrial Revolution, the feedstock used to produce energy from gasification shifted to wood in the 1900s and has now turned to sludge and biosolid waste products. Given its high tolerance for feedstock quality and ability to produce high-grade syngas, plasma gasification, which uses plasma torches as the main heating element, has been favored as an effective method for sewage sludge treatment. Due to the high moisture content of raw sewage sludge, pre-drying procedures are typically required to be embedded in the systems [13]. The entire process with this added step makes for a highly taxing treatment system in terms of heat energy demand. For that reason, it becomes an appropriate technology for a smaller residential scale appliance, while industrial applications offer much greater challenges.

2.2.1 Cranfield Nano-Membrane Toilet

The submission from Cranfield University demonstrated an elegant, compact, well-developed prototype design using gasification. Figure 2.5 shows the cross-sectional schematic of the self-contained appliance.

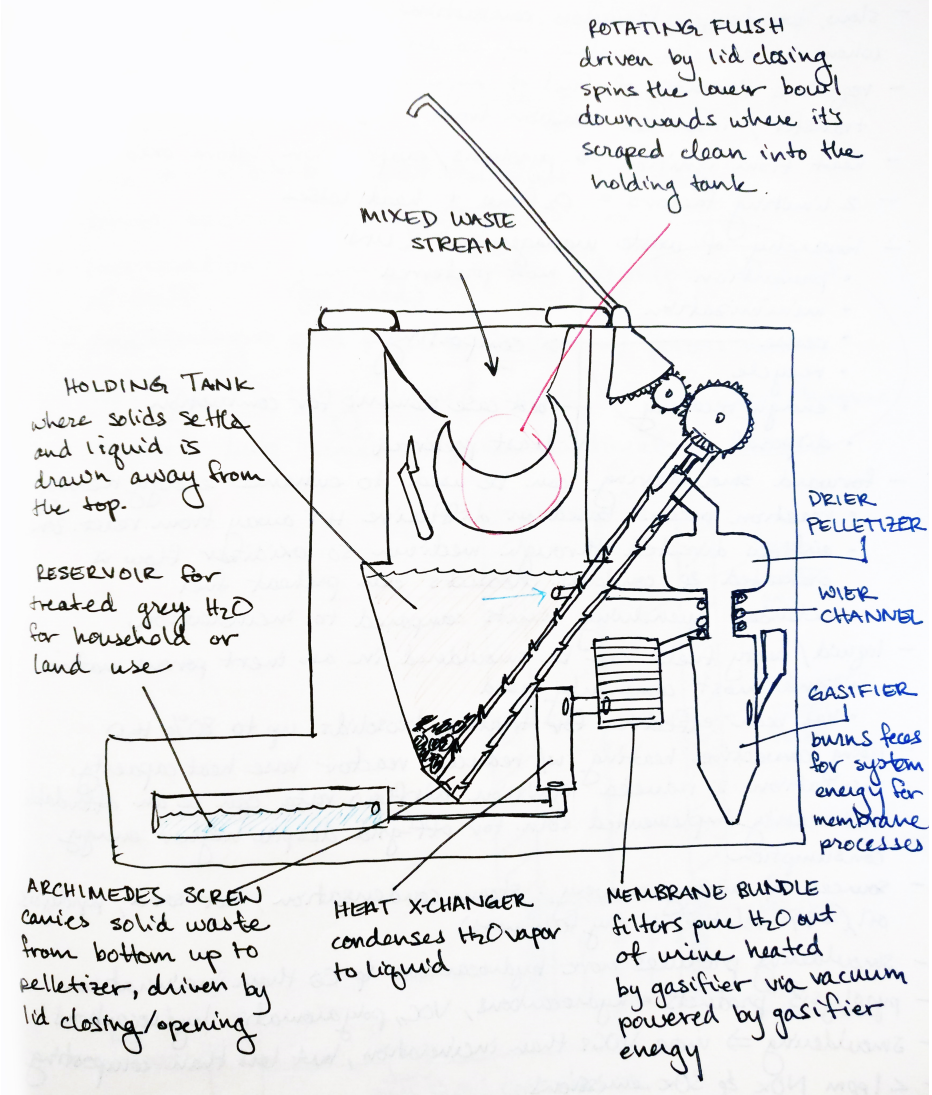

Figure 2.5: Cranfield Nano Membrane Toilet internal system schematic. (Source: Cranfield University)

As the mixed waste stream enters, a rotating flush and scooping mechanism transfers the contents to a mixed media holding tank where primary settling occurs. The

suspended layer of liquid supernatant evacuates the tank through the wier channel, while and Archimedes screw carries the settled solids to the top of the gasification chamber. There, a pelletizer isolates the new batch of fuel as it undergoes the pre-drying process, which is achieved using the hot gas produced from the reaction chamber. This heat is also designed to treat the liquid supernatant using a heat exchanger and by powering the membrane filtration bundle before being stored in the reservoir as treated grey water [27].

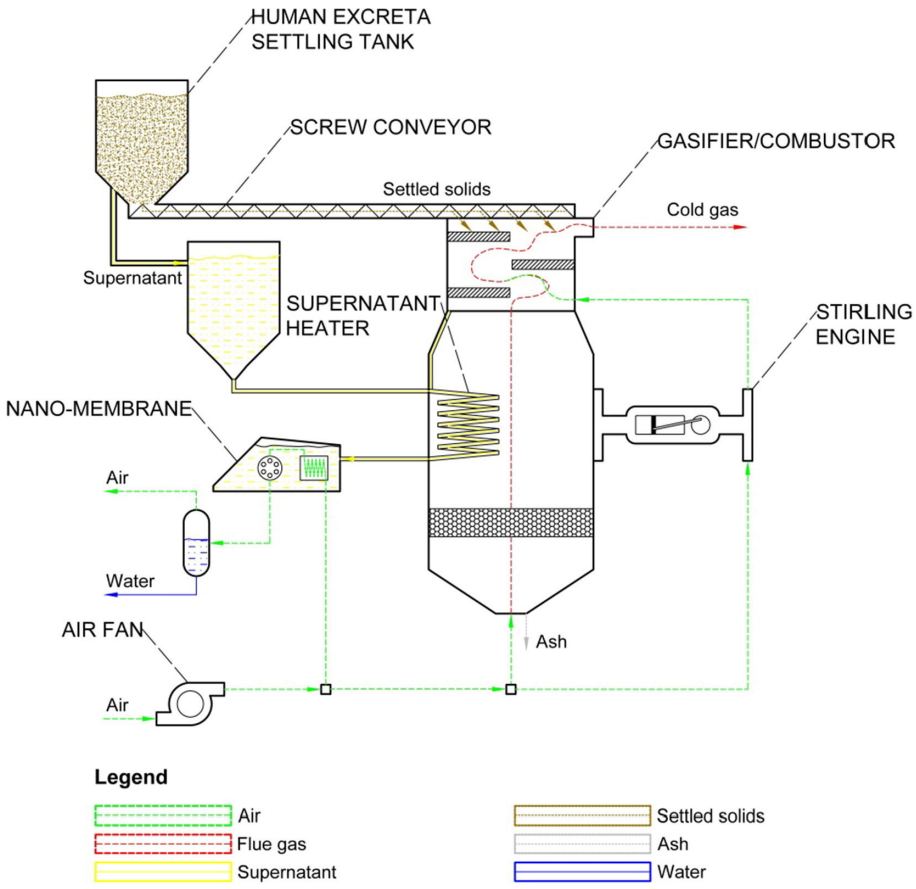

Figure 2.6: Cranfield Nano Membrane Toilet model schematic representation. (Source: Hanak et al.)

A performance evaluation of the Nano Membrane Toilet designed by Cranfield University was published in 2016 by Hanak et al. to confirm the energy self-sustainability

of the system. Using the Aspen Plus® software package, the theoretical electrical energy recovery ability was determined through a thermochemical conversion system connected to a Stirling engine. The net power output, according to their model, suggests 2-6 W, similar to a USB port [6]. It was reported that the energy recovered by the Stirling engine depends on both the moisture content and temperature of solids upon exiting the pre-dryer. Since the released heat also powers the liquid treatment devices, the recovered energy is also dictated by how much supernatant must be processed.

In using a treatment method with a reputable history in this application, the Cranfield Nano-Membrane Toilet has shown quick developmental progress towards a physical prototype. Designs that employ less common waste combustion methods lack the same foundation in understanding, making it more difficult to validate a comprehensive design. The potential for cost and energy savings, however, suggest that these alternatives may be well worth exploring.

2.3 Wastewater Treatment via Smoldering

Having mainly been studied in the area of fire safety, smoldering combustion is defined as the low-temperature, slow-burning, flameless, combustion of a solid fuel. The fuel in question must consist of a porous matrix to create a large surface area for heat transfer and air flow. The resulting air pockets allow the smoldering reaction front to be both insulated and exposed to small amounts of oxygen to sustain the reaction. For waste feeds with a high moisture content, porosity is achieved by mixing it with a granular substance, such as sand, to produce the desired consistency [3]. It has been shown that, while gasification requires a pre-drying process for moist fuels, smoldering can accept fuels of up to 75% moisture content with no additional thermal treatment [6]. In addition, the low combustion temperature and the airflow-controlled

propagation require less energy input to initiate and perform treatment, making it an appealing option for a residential scale.

2.3.1 University of Toronto Reinvent the Toilet Submission

The University of Toronto challenge submission consisted of a self-sustaining unit powered by a smoldering combustion reactor. Figure 2.7 illustrates a cross-section schematic of the conceptual design.

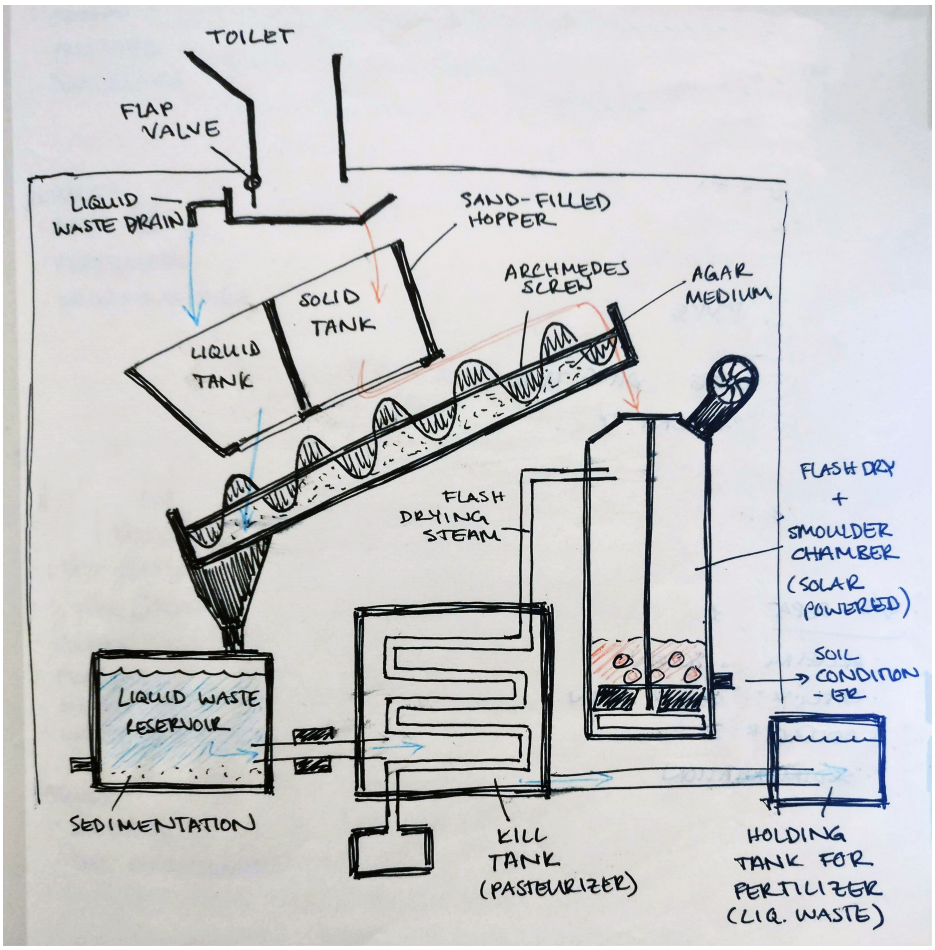

Figure 2.7: University of Toronto smoldering toilet prototype schematic. (Source: University of Toronto)

Starting at the toilet, the waste is separated into a conjoined liquid and solid holding tank, from which the liquids drip into a reservoir and the solids drop onto

an Archimedes screw with an agar medium. The screw moves the solid waste to the top of the smoldering reactor, where it is deposited and manually mixed with sand to create the porous matrix. Using solar energy to power the heating elements at the bottom, the waste is smoldered, leaving only treated sand, which can be reused within the system, and small amounts of ash, which can be used as soil conditioner. The heat from the reaction is simultaneously used to pasteurize the liquid waste, which can then be used as fertilizer [17].

In comparison to gasification, which has been well-researched and practiced in the waste treatment community, sewage smoldering represents a new approach with minimal existing studies. Whereas the gasification prototype included a study using a computer-based model to estimate recoverable energy, the smoldering design only included experimental data on the reactor performance. As a result, the niche for this project appeared with the goal of exploring sewage smoldering modeling methods to boost the credibility of this and other smoldering reactor prototypes.

2.4 Summary of Approach

Using the experimental temperature data collected from the University of Toronto's prototype configuration, this thesis approached the problem with the goal of establishing a preliminary baseline for sewage smoldering simulation. Without pursuing the more complex aspects of smoldering combustion in detail, the smoldering reactor was modeled as a one-dimensional, homogeneous solid. Assumptions regarding the physical properties of the fuel and the thermal behavior were then applied, such that the model would represent the "most basic" interpretation of the problem. Given that many of the assumptions made reflected ideal circumstances with no heat loss, it was predicted that this study would yield more optimistic results than the experimental data with respect to heat transfer rates, maximum temperatures, and recovered heat

energy.

Once the experimental configuration was defined as a controlled volume and outlined with assumptions, the main heat equations were derived from elementary laws of heat transfer. The transient nature of the experimental results led to the use of finite-difference methods to approximate the temperature profiles within the reactor throughout a batch smoldering process. The derived numerical computation equations were solved using a program written in Matlab. The resulting graphs were tailored for both model and experimental comparison, as well as visualization of the smoldering front propagation. The complete approach and model development theory is covered in the following chapter.

Chapter 3

SMOLDERING COMBUSTION FINITE-DIFFERENCE MODELING

Although smoldering phenomena have previously been studied in contexts such as cigarettes and fire protection [15] [20], the possibility of application as a form of sewage sanitation has only been proposed and tested in the last five years. While experimental findings and the University of Toronto prototype have brought public attention to this subject, furthering the depth of its study will eventually require an analysis of the thermodynamics at work. For the purpose of better understanding the physics behind smoldering as a waste treatment, a parameter-based computer model is desirable for simulating the physical behavior of sewage smoldering experiments.

3.1 Theoretical Model Development

As of the submission of this thesis, no literature has been published on the mathematical or computer-based modeling of smoldering wastewater treatment on a residential scale. The main resources for developing this model, therefore, consisted of experimental data from recent studies on sewage smoldering. With the quantification of thermal energy recovery as the eventual goal for this model, the internal temperature distribution became the parameter of interest. As with any model, assumptions were made to simplify the smoldering process such that governing equations could be derived to describe the basic functions. From there, finite-difference methods were used to approximate temperature profiles at various times within a specified smoldering period. Given that this approach represents the first of its kind for this scale and application, the underlying logic for this model was to simplify the physics down to the bare minimum and observe the level of accuracy that could be obtained. Conse-

quently, some of the typical factors included in other smoldering models, such as fuel porosity and internal fluid dynamics, were not taken into account.

3.1.1 Experimental Parameters and Data for Correlation

The data on which the computational model was based originated from two main experimental studies: *Continuous, self-sustaining smouldering destruction of simulated faeces* by Fabris et al. and *Smouldering combustion as a treatment technology for faeces: Exploring the parameter space* by Yerman et al. [3] [41]. The experiments performed by Fabris et al. in 2016 provided the first demonstration of feasible continuous smoldering combustion for simulated feces in direct relation to the prototype designed by the University of Toronto. Much of the procedure and setup for this study was also based on the second reference by Yerman et al. The work by Yerman et al., published in 2015, offered the first evidence of self-sustaining smoldering as a possible alternative to sewage incineration, in addition to evaluating the effect of various factors on performance. Together, these references provided, not only the data for simulation, but also the physics upon which the computational logic was based.

To better illustrate the concepts within the smoldering experiments, the procedures may be compared to the familiar example of smoking a cigarette. The basic structure can be described as an open-ended column filled with a porous combustible media. Once the cigarette is ignited at the tip, the smoldering reaction requires no additional heat for the tobacco to be consumed. Instead, the smoldering front propagates along the length of the cigarette due to the air drawn in with each inhale. A smoldering apparatus should, therefore, be able to theoretically sustain itself given a column of porous combustible fuel, an initial heat source, and a constant airflow.

The main waste column reactor consisted of a hollow stainless steel cylinder 37.2 cm tall with a 6.25 cm inner diameter, as shown in Figure 3.1. Temperature profiles

were recorded using thermocouples placed along the central axis of the column. At the base, two 200 W cartridge heaters provided the heat flux for ignition, while a fan and mass flow controller regulated the internal airflow used to propagate the reaction up the column. Because the airflow originates from the base and pushes the reaction front forward instead of pulling it up, these experiments employ forward smoldering propagation. The particular experiment modeled for this thesis was Experiment 6 out of the ten performed by Fabris, for which the settings included a 1.85 cm/s airflow rate and a 26.3 cm trigger height. For the airflow to properly influence the internal heat transfer, the fuel must exhibit significant porosity. To obtain the appropriate characteristics, the final fuel recipe contained surrogate feces mixed with silica sand in a 1:24 ratio by mass with a 33% moisture content to produce a porous fuel matrix.

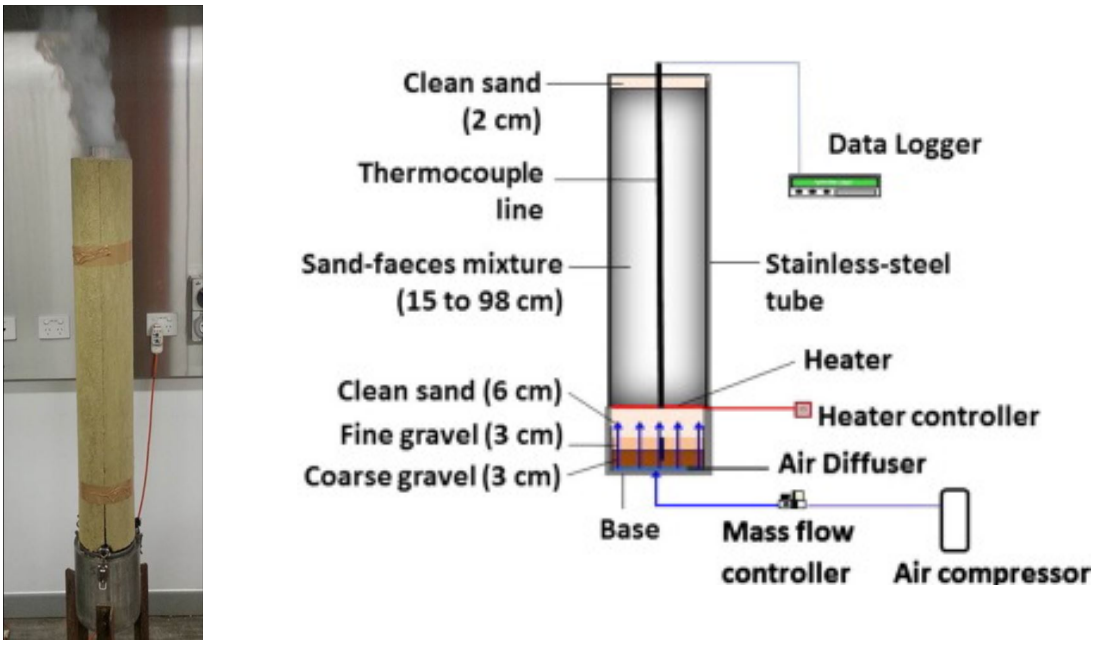

Figure 3.1: Exerimental setup for the experiments performed by Yerman et al.

As depicted in Figure 3.2, each batch of fuel undergoes the same cyclical four-stage procedure: air, propagation, discharge, and resetting. A cycle begins once the base of the waste column has been ignited, which usually occurs after about 90 min of

exposure to the 400 W heat flux provided by the heaters. This moment, represented as $t = 0$, is characterized by an inital temperature profile that shows the smoldering front at the base of the column. From there, stage 1 introduces air flow to begin forcing the reaction front forward. After an average of 2 hours, the thermocouple located at the trigger height 26.3 cm above the base of the column outputs a temperature corresponding with ignition, indicating that the reaction front has reached the top after having consumed most of the fuel in the column. At this point, the air is shut off, and stage 3 proceeds with the manual ejection of the remaining clean sand and the addition of a new batch of virgin fuel. In the fourth and final stage, the fuel assembly is pushed back to the original configuration before the cycle repeats. Although the ejection and repacking of the fuel matrix would have to be integrated into the actual prototype, those stages proved irrelevant for this model, which focuses on performing a simplified analysis of the smoldering physics. As a result, this project only describes the self-sustained portion of each cycle, which occurs between stages 1 and 2, given that no additional heat contributes to moving the reaction front forward.

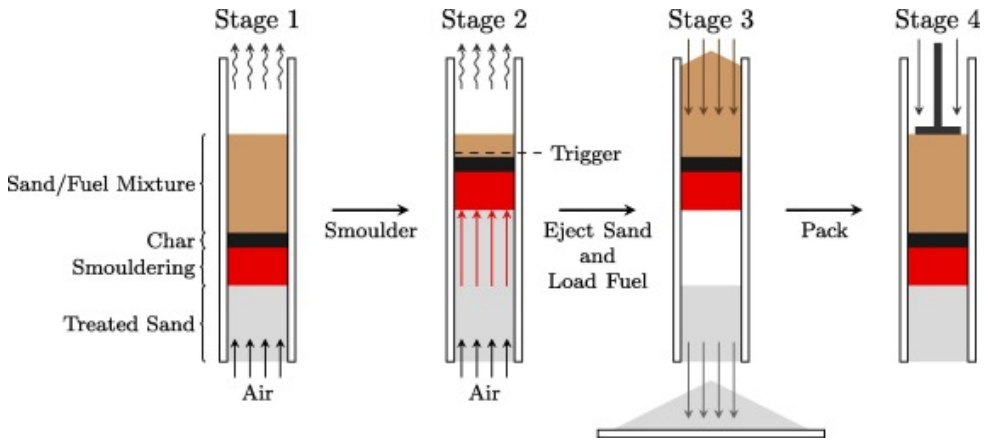

Figure 3.2: The four-stage batch process. Fabris et al. (Fig.2)

The position of the reaction front may be determined for a given time during each smoldering session based on the corresponding temperature profile. Figure 3.3

explains the relationship between thermal zones and the temperature distribution in the waste column. The key point of the diagram shows that the reaction front, located at the transition between the smoldering and pyrolysis zones, is associated with the peak values of the temperature profile. This allows one to locate the reaction front at any given time based on the height at which the maximum temperature occurs.

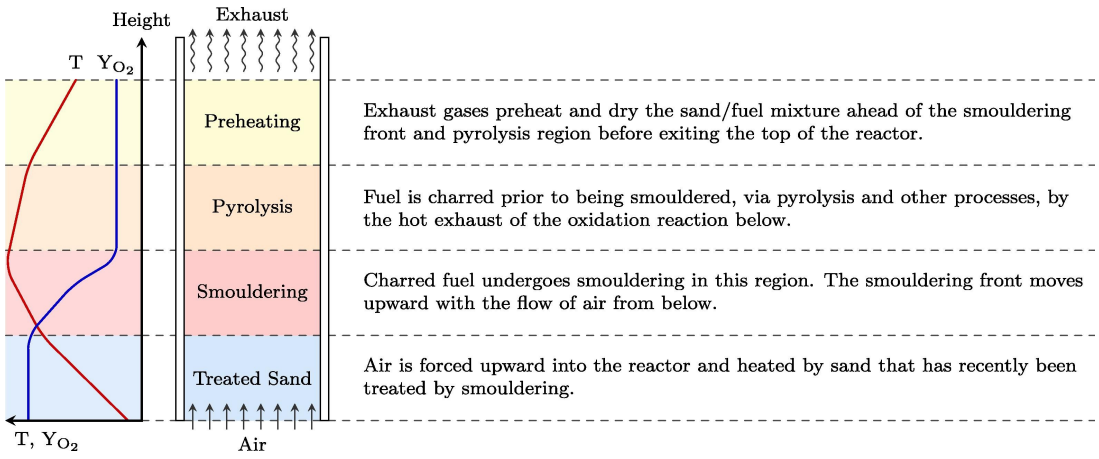

Figure 3.3: Temperature profile correspondence to waste column thermal zones. Fabris et al. (Fig.1)

Given that the target was to replicate temperature profiles, the data in Figure 3.4 became the main reference as the one image that illustrated the reaction front progression using temperature distributions at various times. The red, blue, and green lines represent the temperature profiles from heater ignition up to the end of the first cycle in Experiment 6 (E6) by Fabris et al. Using a typical batch process, which takes roughly 2 hours to complete a full cycle for this scale, the profiles were shown for three time steps within the last 40 minutes of the batch smoldering. The location of the reaction front can easily be identified for each time step as the x-value corresponding to the last data point before the sharp downwards slope (i.e. $x = 11$ cm for $t = 80$ min). Over time, the visible movement of the reaction front is demonstrated by the fact that the colored graphs shift to the right by about 6 cm every 20 min. Based on the

resulting velocity of the smoldering front and the fuel density of the porous fuel matrix, the mass destruction rate of dry fuel was recorded as 27.5 grams per hour for E6.

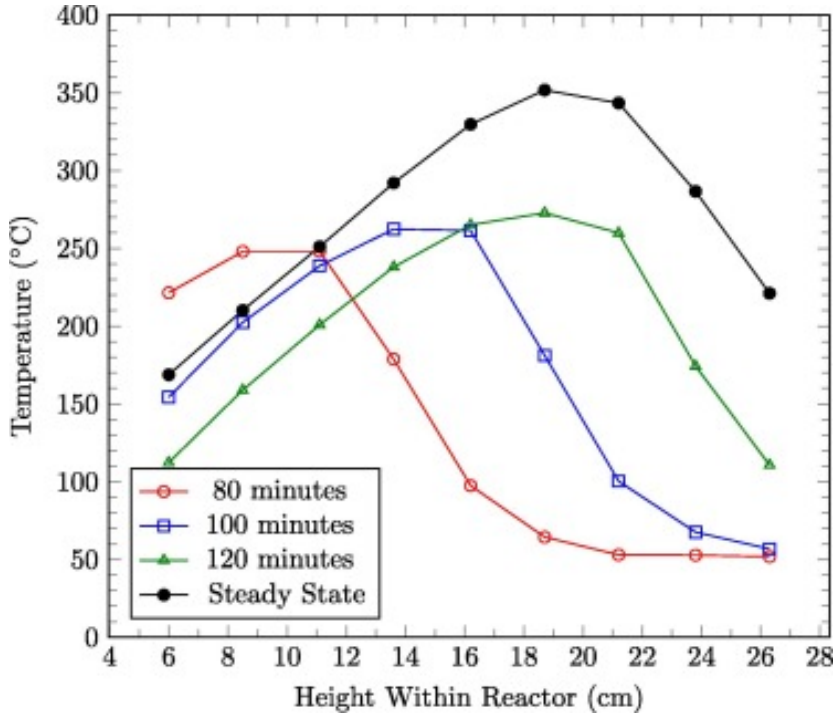

Figure 3.4: Batch process sewage smoldering progression data. Fabris et al. (Fig.6)

Note: The steady state data in this graph is not relevant to this study.

The black line shows the results for a continuous, quasi-steady state process, which is only achieved after 9 to 16 cycles have run in constant succession. Although experimentally, this method can reduce the duration of each cycle down to an average of roughly 17.5 min for this scale, it is not relevant to this study due to procedural complexity. Modeling this process would have required taking additional operational factors into account, making for a more complicated model that could be better simulated in future studies (see Chapter 6).

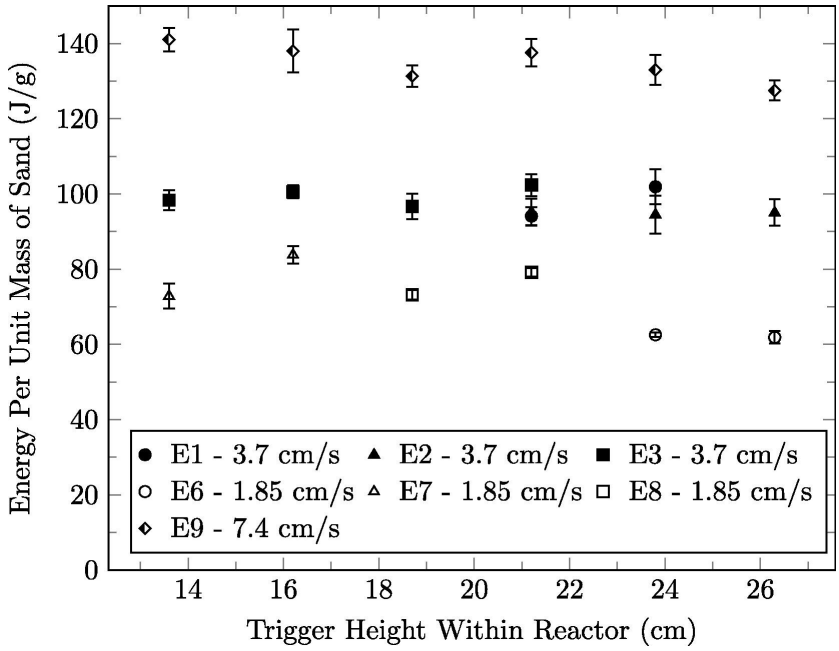

Figure 3.5: Batch process sewage smoldering ejected energy data. Fabris et al. (Fig.9)

Ultimately, the recoverable thermal energy from the hot treated sand was determined by using it to heat a known mass of water. It is known that, when two substances (A and B) with different temperatures are combined, the change in internal energy of one substance is equal to the change in internal energy of the other as a function of the change in temperature:

$$(mc\Delta T)_A = (mc\Delta T)_B$$

Knowing the mass and heat capacity of the treated sand and the vat of water, the thermal energy transferred from the hot sand to the water was calculated based on experimental temperature values. The findings suggested a specific recoverable heat energy range of 60 to 140 joules per gram of hot sand for each ejection. Since this model worked specifically with the values from E6, the corresponding recovered energy to match was on the lower end of that range at about 61 J/g of hot sand, as shown by the bottom-right data point in Figure 3.5.

Having outlined the basis for the model based on experimental results, the next step in reducing the physical behavior to simplified governing equations required the statement of the proper assumptions.

3.1.2 Assumptions

As with most heat transfer models, the first task in describing the problem was to establish a control volume and identify inputs and outputs. The control volume was designated to include only the sewage column within the stainless steel cylinder, ignoring the properties of the actual container and focusing specifically on the the media undergoing combustion. Since the experimental apparatus included features to maximize insulation along the length of the column, the lateral boundary of the waste column was assumed to be perfectly insulated, or adiabatic, such that no heat could be transferred across the sides. The open ends of the waste column were assumed to be subjected to specific boundary conditions at each end. The base of the column would mainly experience convection losses due to direct contact with the forced airflow. The top of the column configuration opens directly to the surrounding environment, for which the ambient temperature is much lower than the virgin fuel temperatures. As a result, the top boundary experiences losses due to both convection and radiation. Radiation effects at the bottom of the column are negated since the actual experimental configuration remains slightly enclosed from the ambient surroundings to direct airflow. Because the heaters take over an hour to ignite the virgin fuel, it can be assumed that the environment in direct contact with the base boundary has a comparable temperature to that of the virgin fuel and the radiation effects have much less influence compared to the convection effects. The convective heat transfer phenomena the occurs within the porous media due to the forced airflow, however, was not handled in terms of the higher level fluid dynamics typically required for a detailed analysis.

Because the moving reaction boundary constitutes the key effect of the forced airflow, its influence was accounted for by treating the fuel matrix as a homogeneous, isotropic solid with constant properties and uniform heat generation. Because of the porous nature of the fuel, airflow is required to propagate the reaction and continuously consume the fuel. For a solid with isotropic thermal properties, however, conductive heat transfer occurs continuously through the media, such that the temperature at one location affects the surrounding temperatures in the solid. It is, therefore, expected that the temperature distribution and reaction front progression would be comparable if the airflow through smoldering porous media were modeled as a heat-generating isotropic solid. Within the fuel matrix, sand constitutes the majority of the dry mass at a 24:1 ratio with the sewage solids, while water makes up 33% of the matrix. The fuel matrix was then assumed to be a homogeneous solid with the thermal property values, k and c_p, of wet sand. Physical and combustion properties were determined from the experimental setup and results. The property values used during computation are listed below [25]:

$$\rho = 2.122 \text{ grams per cubic centimeter}$$

$$c_p = 0.83 \text{ joules per gram per } ^\circ\text{C}$$

$$k = 2 \text{ watts per meter per } ^\circ\text{C}$$

$$H_c = 20.6 \text{ kilojoules per gram}$$

$$\dot{m} = 27.5 \text{ grams per hour}$$

One-dimensional transient heat transfer was assumed due to the experimental set up and method for data collection. The values graphed in Figure 3.4 were obtained from thermocouples situated along the central axis of the waste column, which only allows for the recording of a temperature gradient relative to one dimension. Furthermore, the measures taken to insulate the apparatus on the lateral boundary confirm

that the radial temperature losses can be considered negligible, resulting in a uniform cross-sectional temperature.The initial list of model assumptions reads as follows:

- Boundary conditions exist at the top and base of the column.
- The lateral boundaries are perfectly insulated (adiabatic).
- The porous fuel matrix is defined as a homogeneous, isotropic solid with constant properties.
- The property values for the fuel matrix are equal to wet sand.
- Only one-dimensional transient heat transfer occurs along the central axis.
- The cross-sectional temperature distribution is uniform.

3.1.3 Governing Heat Equation Derivations

Once the control volume was established, the general equations used to describe the transient changes in temperature distribution were derived using the energy balance method. The volume in question can be considered to be composed of an infinite number of cubic elements. For any element, the energy stored within a body is determined by the net heat flux through the body, in addition to any energy generated by the body. The rate of change of internal energy for a given element can, thus, be defined by the following equation [10]:

$$\dot{E}_{stored} = \dot{E}_{net} + \dot{E}_{gen} \tag{3.1}$$

where $\dot{E}_{net} = \dot{E}_{in} - \dot{E}_{out}$. To put each term in the context of heat, Q, the following definitions are applied:

$$\frac{\text{heat stored}}{\text{unit volume}} : \frac{q_{stored}}{dV} = Q_{stored} \qquad \frac{\text{heat}}{\text{unit area}} : \frac{dq_i}{dA} = Q_i \qquad \frac{\text{heat gen}}{\text{unit volume}} : \frac{q_{gen}}{V} = Q'$$

Because constant thermal properties are assumed for the entire control volume, it is also assumed that heat is stored and generated uniformly in relation to the entire elemental body. The terms Q_{stored} and Q', therefore, apply per unit volume. The heat flux, however, is only uniform with respect to the cross sectional area while the value changes as a function of axial position, making Q_i specific per unit area. The 3-dimensional theoretical heat flux for a given cubic element within the control volume is visualized in Figure 3.6.

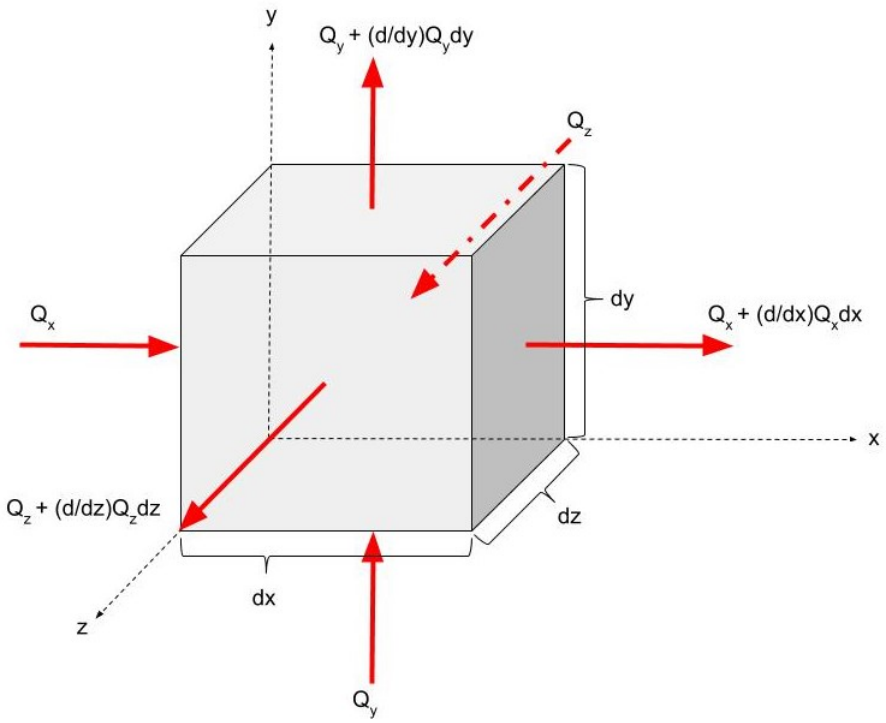

Figure 3.6: 3D node element with heat transfer flow.

Because of the one-dimensional assumption, the only terms from Figure 3.6 present in the heat flux term, $\dot{E}_{net}$, include those acting in the x-direction. To specify direction in equations, standard practice denotes heat transfer from a higher to a lower temperature as positive. The terms from (3.1) can, then be defined as follows,

Net Heat Flux through Elemental Surface: x-direction (see Fig. 3.6)

$$\dot{E}_{net} = \left[-Q_x + \left(Q_x + \frac{\partial}{\partial x} Q_x \partial x \right) \right] \partial y \partial z = \frac{\partial}{\partial x} Q_x \partial x \partial y \partial z$$

Elemental Heat Generated: $\dot{E}_{gen} = Q' \partial x \partial y \partial z$

Time Rate of Change of Elemental Stored Energy:

$$\dot{E}_{stored} = \frac{\partial}{\partial t}(Q_{stored}) \partial x \partial y \partial z$$

such that the original equation becomes,

$$\frac{\partial}{\partial t}(Q_{stored}) \partial x \partial y \partial z = \frac{\partial}{\partial x} Q_x \partial x \partial y \partial z + Q' \partial x \partial y \partial z$$

The thermal energy stored within a body is characterized by the familiar equation $q_{stored} = mc_p dT = V \rho c_p dT$. Using this definition to replace Q_{stored} results in the following,

$$Q_{stored} = \frac{q_{stored}}{V} = \rho c dT$$
$$\frac{\partial}{\partial t}(Q_{stored}) = \rho c_p \frac{\partial T}{\partial t}$$

Plugging that into the heat balance equation, the final product results in the *one-dimensional general heat equation* for elemental heat transfer analysis within the established control volume:

$$\boxed{\rho c_p \left(\frac{\partial T}{\partial t} \right) \partial x \partial y \partial z = \frac{\partial}{\partial x} Q_x \partial x \partial y \partial z + Q' \partial x \partial y \partial z} \tag{3.2}$$

For each nodal element, the heat transfer term Q_x constitutes the sum of the heat transfer modes present through that element, for which there are three options: conduction, convection or radiation. When summing these terms, heat transfer into the node is considered positive. Q_x for each condition is defined as follows:

Rate of 1-D Conduction (Fourier's Law):

$$Q_{x,cond} = -k \frac{\partial T}{\partial x} \tag{3.3}$$

Rate of Convection (Newton's Law of Cooling):

$$Q_{x,conv} = h(T_s - T_\infty) \tag{3.4}$$

Net Rate of Radiation:

$$Q_{x,rad} = \varepsilon\sigma(T_s^4 - T_\infty^4)$$

While the first two laws can be used as is, the radiation equation can be rearranged as follows to be represented by a linear function of temperature instead of a fourth degree function:

$$\begin{aligned} Q_{x,rad} &= \varepsilon\sigma(T_s^4 - T_\infty^4) \\ &= \varepsilon\sigma(T_s + T_\infty)(T_s^2 + T_\infty^2)(T_s - T_\infty) \end{aligned}$$

By designating the *Radiation Heat Transfer Coefficient* such that

$$h_r = \varepsilon\sigma(T_s + T_\infty)(T_s^2 + T_\infty^2),$$

the linearized Net Rate of Radiation becomes:

$$Q_{x,rad} = h_r(T_s - T_\infty) \tag{3.5}$$

Along the waste column, each node can be classified in one of three cases. These provide the boundary conditions for determining the particular heat equations for each node. The first case represents a surface node at the base of the waste column. Here, it is assumed convective heat transfer exists due to contact with the airflow, in addition to conductive heat transfer with the adjacent node. For the second case, which describes the internal nodes within the waste column, only conductive heat transfer is present. Lastly, the third case models a surface node at the top opening of the column. This node experiences conductive heat transfer from the previous node, as well as convection and radiation due to contact with the surrounding environment. Figure 3.7 illustrates the three possible cases.

For any surface element, the model is configured such that the central node is situated at the surface. As a result, the heat storage and generation terms only apply to half the nodal volume, such that $\partial x = \frac{\Delta x}{2}$, as shown in Figure 3.7. This relation is seen in the following derivations of the particular solutions for the two cases pertaining to surface nodes, Case 1 and Case 3. Otherwise, for an internal node, $\partial x = \Delta x$ and $\partial y \partial z = A_c$, the cross-sectional area, for all cases.

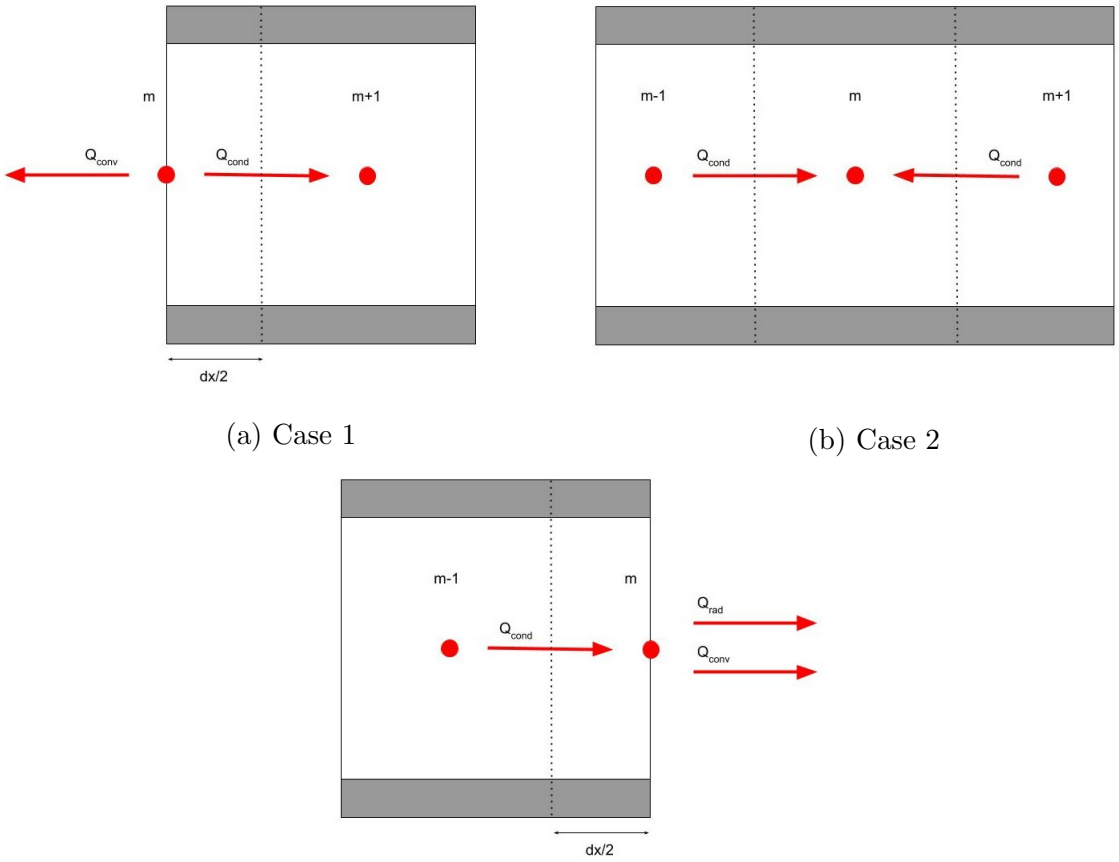

(a) Case 1

(b) Case 2

(c) Case 3

Figure 3.7: Three possible nodal element cases.

Case 1: Surface Element at the Base of the Column

Summing the heat through the base surface node in Figure 3.7a gives,

$$\begin{aligned}\sum Q_x &= -Q_{x,cond} - Q_{x,conv} \\ &= -(-k\frac{\partial T}{\partial x}) - h(T_s - T_\infty) \\ Q_{x,1} &= k\frac{\partial T}{\partial x} - h(T_s - T_\infty) \end{aligned} \tag{3.6}$$

Plugging (3.6) back into the general heat equation results in the following:

$$\begin{aligned}\rho c_p\left(\frac{\partial T}{\partial t}\right)\partial x\partial y\partial z &= \frac{\partial}{\partial x}Q_{x,1}\partial x\partial y\partial z + Q'\partial x\partial y\partial z \\ &= \frac{\partial}{\partial x}\left(k\frac{\partial T}{\partial x} - h(T_s - T_\infty)\right)\partial x\partial y\partial z + Q'\partial x\partial y\partial z \\ \rho c_p\left(\frac{\partial T}{\partial t}\right)\frac{\Delta x A_c}{2} &= \frac{\partial}{\partial x}\left(k\frac{\partial T}{\partial x} - h(T_s - T_\infty)\right)\Delta x A_c + Q'\frac{\Delta x A_c}{2}\end{aligned}$$

This reduces to the following particular solution to the heat equation for Case 1,

$$\boxed{\frac{\rho c_p}{2}\left(\frac{\partial T}{\partial t}\right) = k\frac{\partial}{\partial x}\left(\frac{\partial T}{\partial x}\right) - h\frac{\partial}{\partial x}(T_s - T_\infty) + \frac{Q'}{2}} \tag{3.7}$$

Case 2: Internal Element

This case assumes that the internal element at hand absorbs the conductive heat transfer from both adjacent elements, such that heat flows from element $(m+1)$ and $(m-1)$ to element (m).

$$\begin{aligned}\sum Q_x &= Q_{x,cond} + Q_{x,cond} \\ Q_{x,2} &= -k\frac{\partial T}{\partial x}\bigg|_{m,m-1} - k\frac{\partial T}{\partial x}\bigg|_{m,m+1}\end{aligned} \tag{3.8}$$

(3.8) into (3.2),

$$\begin{aligned}\rho c_p\left(\frac{\partial T}{\partial t}\right)\partial x\partial y\partial z &= \frac{\partial}{\partial x}Q_{x,2}\partial x\partial y\partial z + Q'\partial x\partial y\partial z \\ &= \frac{\partial}{\partial x}\left(-k\frac{\partial T}{\partial x}\bigg|_{m,m-1} - k\frac{\partial T}{\partial x}\bigg|_{m,m+1}\right)\partial x\partial y\partial z + Q'\partial x\partial y\partial z \\ \rho c_p\left(\frac{\partial T}{\partial t}\right)\Delta x A_c &= \frac{\partial}{\partial x}\left(-k\frac{\partial T}{\partial x}\bigg|_{m,m-1} - k\frac{\partial T}{\partial x}\bigg|_{m,m+1}\right)\Delta x A_c + Q'\Delta x A_c\end{aligned}$$

The particular solution to the heat equation for Case 2 then becomes,

$$\boxed{\rho c_p\left(\frac{\partial T}{\partial t}\right) = -k\frac{\partial}{\partial x}\left(\left.\frac{\partial T}{\partial x}\right|_{m,m-1} + \left.\frac{\partial T}{\partial x}\right|_{m,m+1}\right) + Q'} \tag{3.9}$$

Case 3: Surface Element at the Top of the Column

The last case features a surface element at the top of the column that absorbs conductive heat transfer and experiences convection and radiation losses.

$$\begin{aligned}\sum Q_x &= Q_{x,cond} - Q_{x,conv} - Q_{x,rad} \\ Q_{x,3} &= \left(-k\frac{\partial T}{\partial x}\right) - h(T_s - T_\infty) - h_r(T_s - T_\infty)\end{aligned} \tag{3.10}$$

(3.10) into (3.2),

$$\begin{aligned}\rho c_p\left(\frac{\partial T}{\partial t}\right)\partial x\partial y\partial z &= \frac{\partial}{\partial x}Q_{x,3}\partial x\partial y\partial z + Q'\partial x\partial y\partial z \\ &= \frac{\partial}{\partial x}\left[\left(-k\frac{\partial T}{\partial x}\right) - h(T_s - T_\infty) - h_r(T_s - T_\infty)\right]\partial x\partial y\partial z + Q'\partial x\partial y\partial z \\ \rho c_p\left(\frac{\partial T}{\partial t}\right)\frac{\Delta x A_c}{2} &= \left[-k\frac{\partial}{\partial x}\left(\frac{\partial T}{\partial x}\right) - h\frac{\partial}{\partial x}(T_s - T_\infty) - h_r\frac{\partial}{\partial x}(T_s - T_\infty)\right]\Delta x A_c + Q'\frac{\Delta x A_c}{2}\end{aligned}$$

The resulting particular solution to the heat equation for Case 3 then becomes,

$$\boxed{\frac{\rho c_p}{2}\left(\frac{\partial T}{\partial t}\right) = -k\frac{\partial}{\partial x}\left(\frac{\partial T}{\partial x}\right) - h\frac{\partial}{\partial x}(T_s - T_\infty) - h_r\frac{\partial}{\partial x}(T_s - T_\infty) + \frac{Q'}{2}} \tag{3.11}$$

Equations (3.7), (3.9), and (3.11) provide the baseline mathematical descriptions for the behavior associated with the sewage smoldering experiments with respect to temperature distribution over time. Although these may demonstrate an oversimplification of the real-life phenomena, they are appropriate for exploring whether an elementary heat transfer model can sufficiently simulate the behavior of this particular experiment. Despite being composed of basic concepts, to derive solutions for

these equations would present a tedious task. Numerical approximations, therefore, became an attractive option for solving these problems.

3.2 Finite-Difference Model Development

In the field of heat transfer, finite-difference methods are often used to determine numerical approximations to differential problems, by replacing the differential terms with elemental difference terms. Working on a per element scale, the established control volume was defined in terms of a nodal mesh. For one-dimensional computation, this mesh divided the length of the column into a pre-determined number of sections, where each section constituted one element, or node. The width of each element corresponded to the differential term ∂x, which can be approximated as Δx in centimeters, as expressed in the previous section. The total duration of the experiment was also represented by a pre-determined number of time steps, where the increments corresponded with ∂t, which can be approximated as Δt in hours. Together, Δx and Δt defined the mesh size applied to the control volume for the purpose of finite-difference numerical approximation.

To condense the number of terms within each equation, the following constants were introduced,

$$\alpha = \frac{k}{\rho c_p} \qquad \text{(thermal diffusivity)}$$

$$Fo = \frac{\alpha \Delta t}{(\Delta x)^2} \qquad \text{(Fourier number)}$$

$$Bi = \frac{h \Delta x}{k} \qquad \text{(Biot number)}$$

$$2BiFo = \frac{2h\Delta t}{\rho c_p \Delta x}$$

The Fourier number, Fo, plays an important role in finite-difference modeling as a descriptive parameter for the mesh refinement. As a result, it is a common parameter to study for an indication of a model's stability. In the interest of later validating

this model, the finite-difference assumptions were made such that the smoldering experiment approximations would satisfy the consistency condition (see Chapter 5). The following relation was, therefore, assumed to be true:

$$\Delta x_i = g_i(\Delta t), \quad i = 1, 2, ..., d$$

Using the Fourier correlation, Δx could then be defined as a function of Δt as follows:

$$\Delta x = \sqrt{\frac{\alpha \Delta t}{Fo}}$$

with Δt and Fo having user-assigned values during implementation. Proper selection of these values is covered in further detail in Chapter 5.

3.2.1 Implicit Finite-Difference

Two methods exist for calculating finite-difference approximations: The explicit and the implicit method. Explicit finite-difference performs a forward difference approximation, where the temperature for any given node at a time $t = p + 1$ is calculated based on temperature values in the previous time step, $t = p$. Although this method provides a more straight-forward computational procedure, the stability of explicit models is limited to Fo values below 0.5 for a one-dimensional interior node [10]. Unfortunately, this reduces the allowable range of time divisions one can reliably test on their model. In addition, for a given time step, the temperature at one node has no dependence on the temperature of its surrounding nodes at the same moment in time. On the other hand, the implicit method features unconditional stability due to its backwards difference computational approach. For the implicit method, the partial derivatives are approximated as follows:

$$\begin{aligned}
\frac{\partial}{\partial x} &\approx \frac{1}{\Delta x} \\
\left.\frac{\partial T}{\partial t}\right|_m &\approx \frac{T_m^{p+1} - T_m^p}{\Delta t} \\
\left.\frac{\partial T}{\partial x}\right|_{m+1,m} &\approx \frac{T_{m+1}^{p+1} - T_m^{p+1}}{\Delta x} \qquad \text{(evaluated at t = p+1)}
\end{aligned}$$

For a backwards difference approach, the temperature-position derivative is evaluated at the current time, $t = p + 1$, instead of at the previous time step, $t = p$, as shown in the previous equations. This produces a system of equations, one for each node, that must be solved simultaneously as a matrix to determine the new temperature profile. The temperature at one node, therefore, depends also on the temperature of its surrounding nodes at the same time step, all of which are calculated based on the temperature profile for the previous time step using matrix algebra [10].

By implementing the new condensed constants, the particular solutions for each case, (3.7), (3.9), and (3.11) were simplified and rearranged in the following form:

Case 1: Surface Element at the Base of the Column

$$(1 + 2Fo + 2BiFo)T_m^{p+1} - 2FoT_{m+1}^{p+1} = 2BiFoT_\infty + T_m^p + \frac{Q'\Delta t}{\rho c} \tag{3.12}$$

Case 2: Internal Element

$$(1 + 2Fo)T_m^{p+1} - Fo(T_{m-1}^{p+1} + T_{m+1}^{p+1}) = T_m^p + \frac{Q'\Delta t}{\rho c} \tag{3.13}$$

Case 3: Surface Element at the Top of the Column

$$\left[1 + 2Fo + 2BiFo\left(1 + \frac{h_r}{h}\right)\right]T_m^{p+1} - 2FoT_{m-1}^{p+1} = 2BiFo\left(1 + \frac{h_r}{h}\right)T_\infty + T_m^p + \frac{Q'\Delta t}{\rho c} \tag{3.14}$$

For Case 3, because the coefficient h_r is a second degree function of the surface temperature T_s at a given time step, it was evaluated at the previous time $t = p$, such that $T_s = T^p$, in order to maintain a linear function of T^{p+1}.

Having derived the appropriate finite-difference equations for the smoldering experiment problem, an initial temperature profile represents the last piece of required information to begin the computation.

3.2.2 Initial Temperature Profile Simulations

Finite-difference approximations perform calculations based on the values for the desired parameters at previous time steps. An initial temperature profile for time $t = 0$ must, therefore, be provided to kick-start the computation. The events leading up to the waste column ignition consist of a 400 watt heat flux provided by the two cartridge heaters over the course of about 90 minutes [3]. At ignition, only the base of the column has reached the 250 °C ignition temperature, while the rest of the column only experiences the heat conducted from that base location over the 90 minute duration. It is, therefore, expected that the initial temperature profile shows a trend resembling logarithmic decay. Two different models were explored to simulate the results of these events: The Semi-Infinite Solid and the Extended Cylindrical Surface.

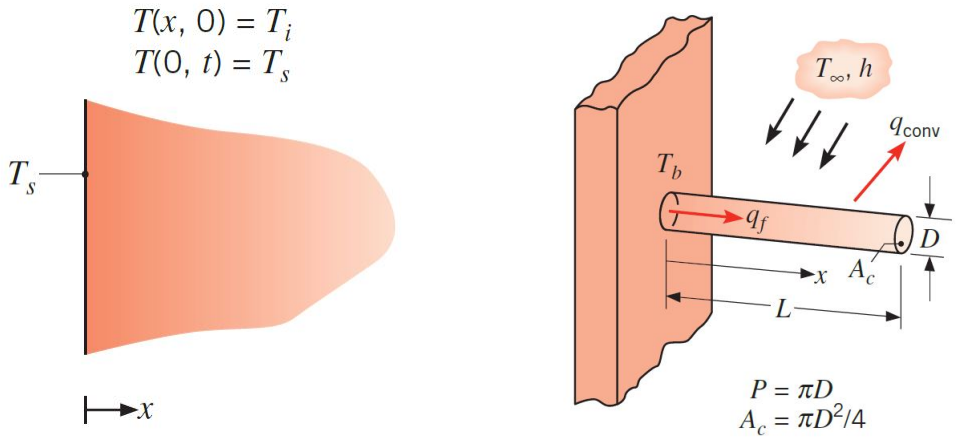

(a) Semi-Infinite Solid w/ Const. Temp.

(b) Extended Cylindrical Fin

Figure 3.8: Visualization of initial temperature models. (Source: F. Incropera)

Initially, the assumption was made that no heat transfer occurs across the lateral column boundary. This allows the column to be treated as a semi-infinite solid in the y and z directions, such that only the x-direction displays a non-uniform temperature

distribution. For a semi-infinite solid with uniform properties and one-dimensional heat transfer, the specific equations have been defined for a few standard cases [10]. Of these, the equation for a constant surface temperature case was used instead of the constant heat flux case. The 400 watt heat flux value was based on the manufacturer's specifications and is more likely to vary overtime and with other factors, whereas the Fabris experimental data confirms that the fuel must reach at least 250 °C before self-sustaining behavior is observed. Thus, the approximate fuel ignition temperature offered a more reliable constant for temperature calculations than the power rating of 200 watts per heater. The following equation was taken from *Heat and Mass Transfer* by Frank Incropera [10] and describes the 1D constant surface temperature case for semi-infinite solid that was used to produce one of the initial temperature profiles:

Semi-Infinite Solid Model: (Constant Surface Temperature)

$$T(x,t) = (T_f - T_{ig})\text{erf}\left(\frac{x}{2\sqrt{\alpha t}}\right) + T_{ig} \tag{3.15}$$

Another way to view the waste column, just for the time leading up to ignition, was as a standing cylindrical column surrounded by air. Comparing Figure 3.8b with Figure 3.1, the extended surface model provides a more visually comparable three-dimensional model with the actual experimental setup. For this case, however, the insulated lateral boundary assumption results in a linear temperature decay since lateral convection is a key component in this model. To produce the appropriate one-dimensional response from a three-dimensional model, the solution was to assign an equivalent convection coefficient, h_{eq}, in the 3D model to represent the real-life radial heat losses that result in a logarithmic decay pattern for the 1D temperature distribution. This coefficient, h_{eq}, was calculated using convection correlations for a cylinder in free air cross-flow based on the methods outlined in Chapter 7 of the Incropera textbook [10]. Assuming an ambient air velocity of 1 mile per hour, h_{eq} was found to be 9 watts per square meter per °C. For convection heat transfer from

the tip of a fin, the following equation from Chapter 3 of Incropera was applied and used to produce a second option for an initial temperature profile:

Extended Surface Model: (Cylindrical Fin)

$$T(x) = \frac{\cosh\left(m(L-x)\right) + \frac{h_{eq}}{mk}\sinh\left(m(L-x)\right)}{\cosh mL + \frac{h_{eq}}{mk}\sinh mL}(T_{ig} - T_\infty) + T_\infty \tag{3.16}$$

where $m^2 = \frac{4h_{eq}}{kD}$ for a circular cross-section.

The comparison of the results from each model are shown in Figure 3.9. Overall, the models provided rather similar temperature distributions. The main difference came with the extended surface model predicting a more gradual temperature decrease along the column, whereas the semi-infinite solid expected a more abrupt decrease. Because no experimental initial temperature profile was available to determine which model produced more accurate results, the profile used during computation was chosen based on visual comparison with the temperature decay pattern of the experimental data in Figure 3.4. There, the curves exhibit a more gradual decrease in temperature closer to the pattern shown by the extended surface model. From this perspective, the extended surface model results seemed to be the more appropriate values to use. This model, however, should be confirmed with results from future experiments (see Chapter 6) by physically collecting data for the initial temperature profile to better visualize the realistic heat losses along the fin. In addition, the expected recoverable thermal energy values were closer to the experimental predictions when using the extended surface as opposed to the semi-infinite solid model.

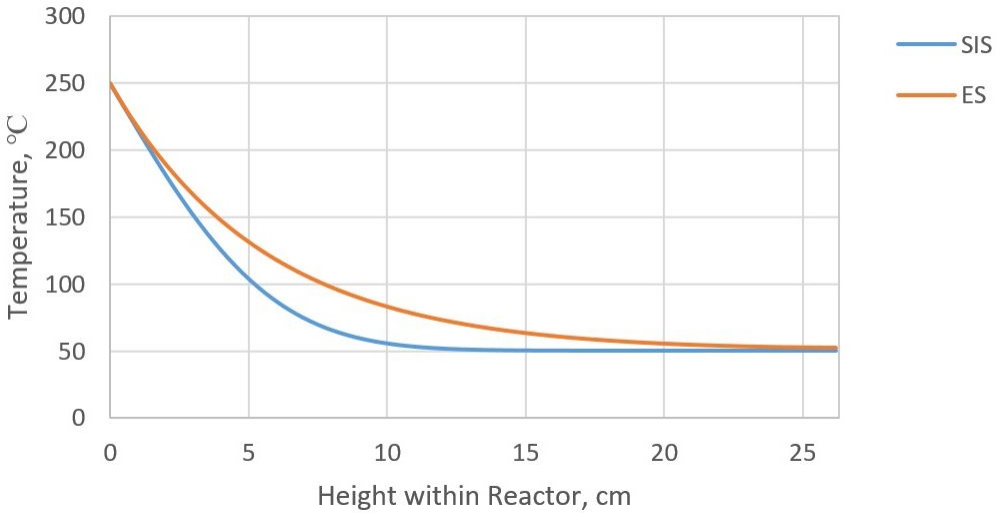

Figure 3.9: Comparison of the initial temperature profiles generated using the semi-infinite solid (SIS) and the extended surface (ES) model.

Having produced a temperature profile for time $t = 0$ and derived and converted the governing equations to implicit finite-difference forms, the next step was to implement the computational logic.

3.2.3 Computational Logic

The temperature effects of heat generation from smoldering combustion were implemented using a series of conditional statements, based on the requirements for smoldering to occur. For any given node within the waste column to be considered eligible for smoldering combustion, the nodal temperature in the previous time step had to be greater than or equal to 250 °C, signifying that ignition has occurred. In addition, each node could only undergo combustion once. Lastly, the location of the node within the waste column determined which equation would be applied based on the three cases shown in Figure 3.7. The resulting diagram in Figure 3.10, depicts the logic flow implemented to account for the three smoldering conditions.

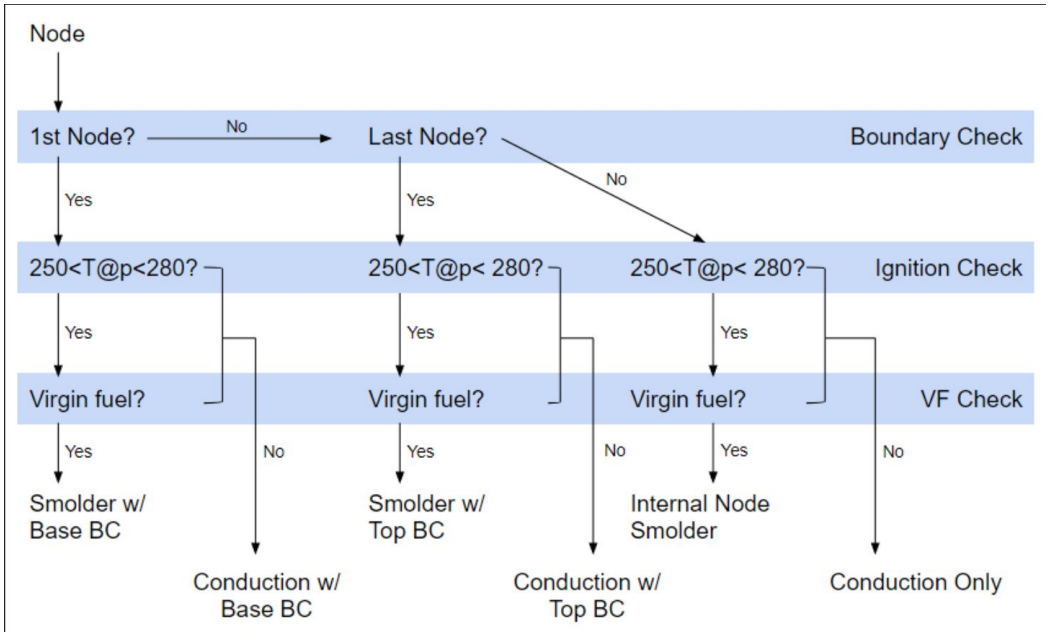

Figure 3.10: Code logic for the computational smoldering conditional statement.

When passed a node for computation, the first conditional statement performed a boundary check, which evaluated whether the current node was at a boundary or in the middle of the column. Determining the nodal location set the program on the appropriate track for computation with the correct equation. From there, the ignition check ensured that the node in question had reached the ignition temperature in the previous time step. To distinguish between nodes generating heat due to combustion versus those experiencing raised temperatures post-combustion, the ignition check threshold was established as a range instead of a single temperature. Arbitrarily, 280°C was selected as the upper limit. This value was selected, assuming a 30°C range was adequate for triggering smoldering after ignition without continuing the reaction in nodes representing hot sand where the fuel had already been consumed. For the final condition, the virgin fuel check was implemented to verify that the node in question had not already undergone combustion. For each nodal position, a virgin fuel marker variable was assigned a boolean value such that '0' indicated virgin fuel

and '1' implied that the fuel within the given node had already been consumed due to smoldering. This value would switch from 0 to 1 for each node as the smoldering front passed through. By checking the marker value for any given node, the virgin fuel check provided the final check to determine smoldering eligibility. Together, the conditional statements, the initial temperature profile, and the implicit-difference equations comprised the computational methodology for this model.

To summarize the modeling strategy, the smoldering experiments from Fabris et al. were simplified into solid control volumes with specialized boundary conditions, from which the governing heat equations were derived. The subsequent equations were then converted to implicit difference forms, such that, for a given time step, the temperatures at each node were calculated simultaneously using system of equation matrices. The initial temperature profile at time $t = 0$ was simulated using a cylindrical extended fin model and provided the computational foundation for the resulting temperature profiles. Lastly, the heat generated due to smoldering was implemented using the three logical statements, which ensured that the proper combustion conditions were met. The following chapter reveals and discusses the best results from the implicit-difference study.

Chapter 4

RESULTS AND DISCUSSION

The results for a Fourier number of 5 were chosen as the best results for reflecting the overall model behavior. The convergence study, which is detailed later in Chapter 5, reveals that the average smoldering reaction temperature for a Fo = 5, shown by the dashed line in Figure 4.1, exhibits the closest value to the average of the same parameter value for other mesh sizes. Figure 4.2 displays the results for the model when using the extended cylindrical surface (ECS) initial temperature profile. When compared with Figure 4.1, however, the ECS approximations appeared to overestimate the length of the smoldering plateau, as well as the rate of temperature decay in the preheating zone, as shown by the abrupt downwards slope. The ECS model data, therefore, was not included as a best result in the discussion that follows. While the best results were also evaluated in terms of visual similarity in graph trends, the main object of interest was the smoldering progression visualization. In order to quantify the progression visualization quality with a single value, the average smoldering reaction temperature per batch was established as the main metric since it aligned well with the smoldering zone plateaus. This average reaction temperature was shown to fluctuate across a 50 degree range with varying mesh sizes, however, the average of these results was best represented by the $277°C$ value for a Fo = 5 using a semi-infinite solid (SIS) initial temperature profile.

For the sake of physical visualization, it is useful to picture the following graphs as lengthwise sectional views of the smoldering reactor with the columns laying on its side. Using this layout, the data was able to be plotted with the y-axis representing temperature as a function of the height within the reactor.

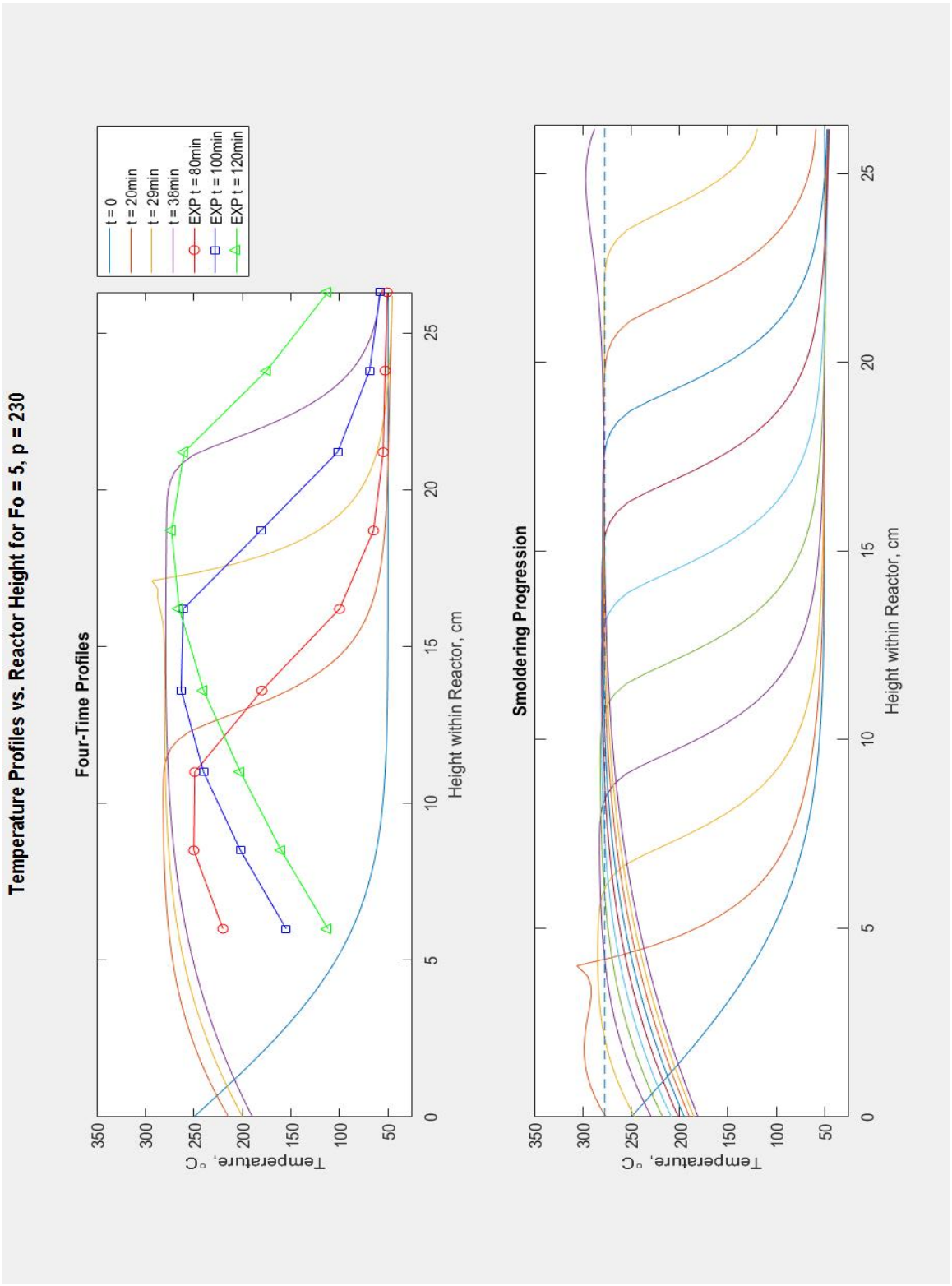

Figure 4.1: Summary of temperature behavior model approximations using a semi-infinite solid initial temperature profile.

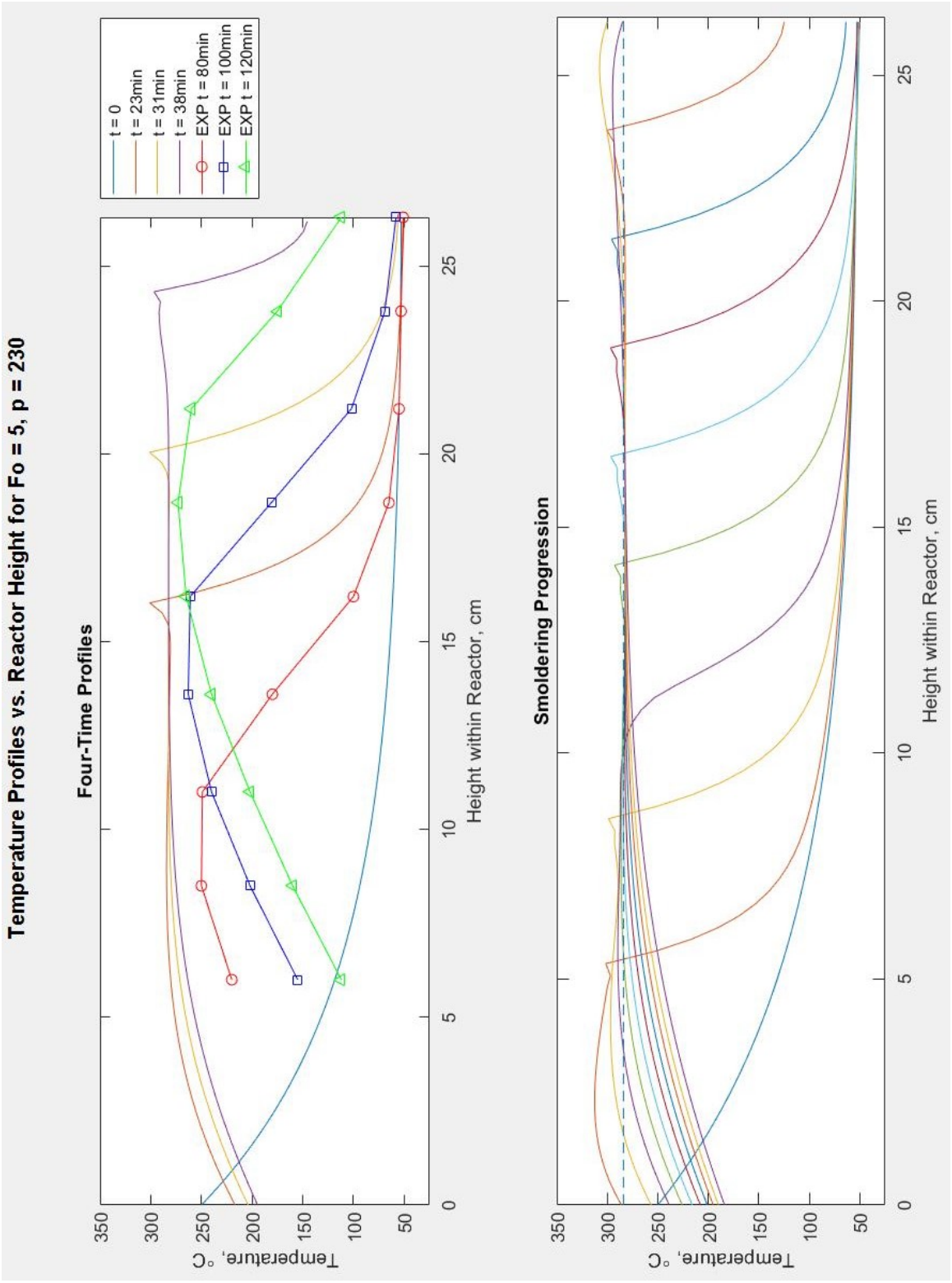

Figure 4.2: Summary of temperature behavior model approximations using an extended cylindrical surface initial temperature profile.

In both Figures 4.1 and 4.2, the top graph compares the model approximations to the experimental data at given stages of the smoldering process. The initial temperature profile used to begin the finite difference calculations is also displayed and labeled in the legend as t = 0. The three profiles were selected to match the experimental data based on the corresponding degree of smoldering progression through the waste column, such that the 22 and 80 minute profiles represent the 50% smoldering completion marks for the theoretical and experimental batch, and so on. Because the graphs are labeled by their time step, it is important to notice that the approximation predicts a much faster smoldering rate than the observed experimental rate by nearly 68-75%. While this presents a large margin of error, it still remains reasonable to expect this result due to the simplifying assumptions made regarding system insulation. Since the lateral boundaries were treated as adiabatic and the model only accounted for one-dimensional heat transfer, the radial losses and imperfect insulation that occur in reality would reduce the rate of the smoldering progression, potentially by that much. The time discrepancy, therefore, is significant, yet expected. On the other hand, the major trend characteristics, such as the reaction temperature plateau height and duration, the smoldering front location and the rate of temperature decay, maintain strong visual similarities to the experimental data.

The second graph in Figure 4.1 provides a more complete image for combustion visualization. From the time of ignition at the base to the time at which the smoldering front reached the top of the column, ten temperature profiles were displayed at even time intervals. The even displacement of the smoldering front overtime, represented by the end of the plateau just before the temperature drop, implies a constant smoldering velocity resulting from the steady state heat transfer assumption made to simplify the model. The similar trend exhibited by the experimental data confirms that this was a reasonable assumption.

4.1 Individual Profile Comparisons

When comparing the time profiles for each smoldering completion percentage, the similarities between the two can be seen in greater detail. Because the experimental data only exists for the locations at which thermocouples were placed, the actual location of the experimental smoldering front between the bounding thermocouples is unknown. To ensure comparison between the experimental data and its best fit approximation profile, the location of the smoldering front used to calculate a percentage was designated as the average value between the bounding thermocouple positions. For example, since Figure 4.3 shows the edge of the plateau at 11.1cm, the actual smoldering front may reside between 11.1 and 13.6 cm. The resulting median is 12.35 cm, which corresponds to 47% of the 26.3 cm waste column length.

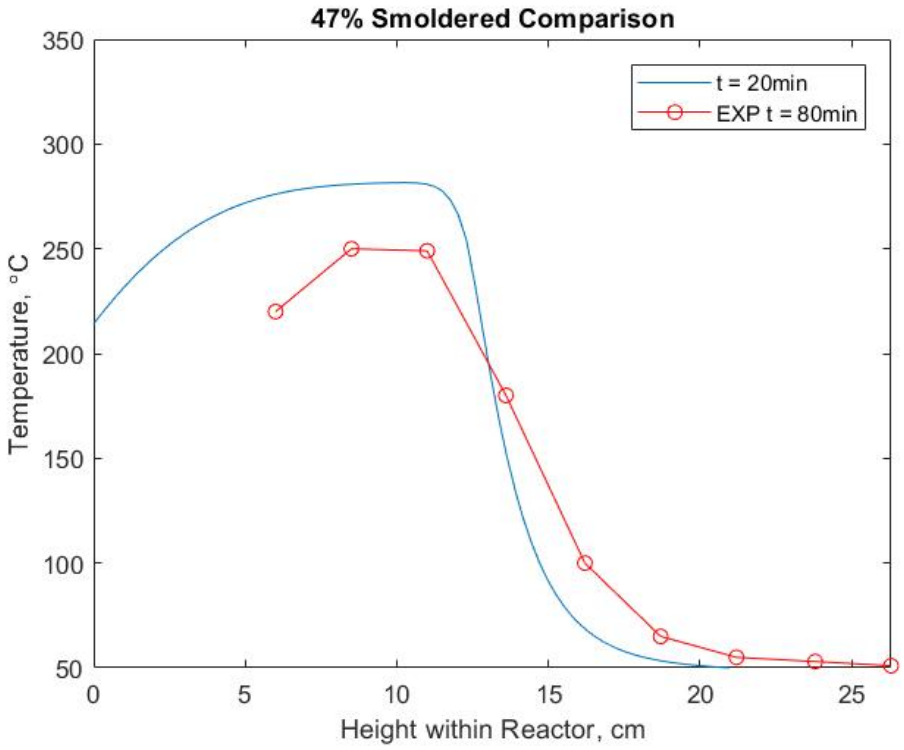

Figure 4.3: Comparison of the temperature profiles at 47% smoldering completion.

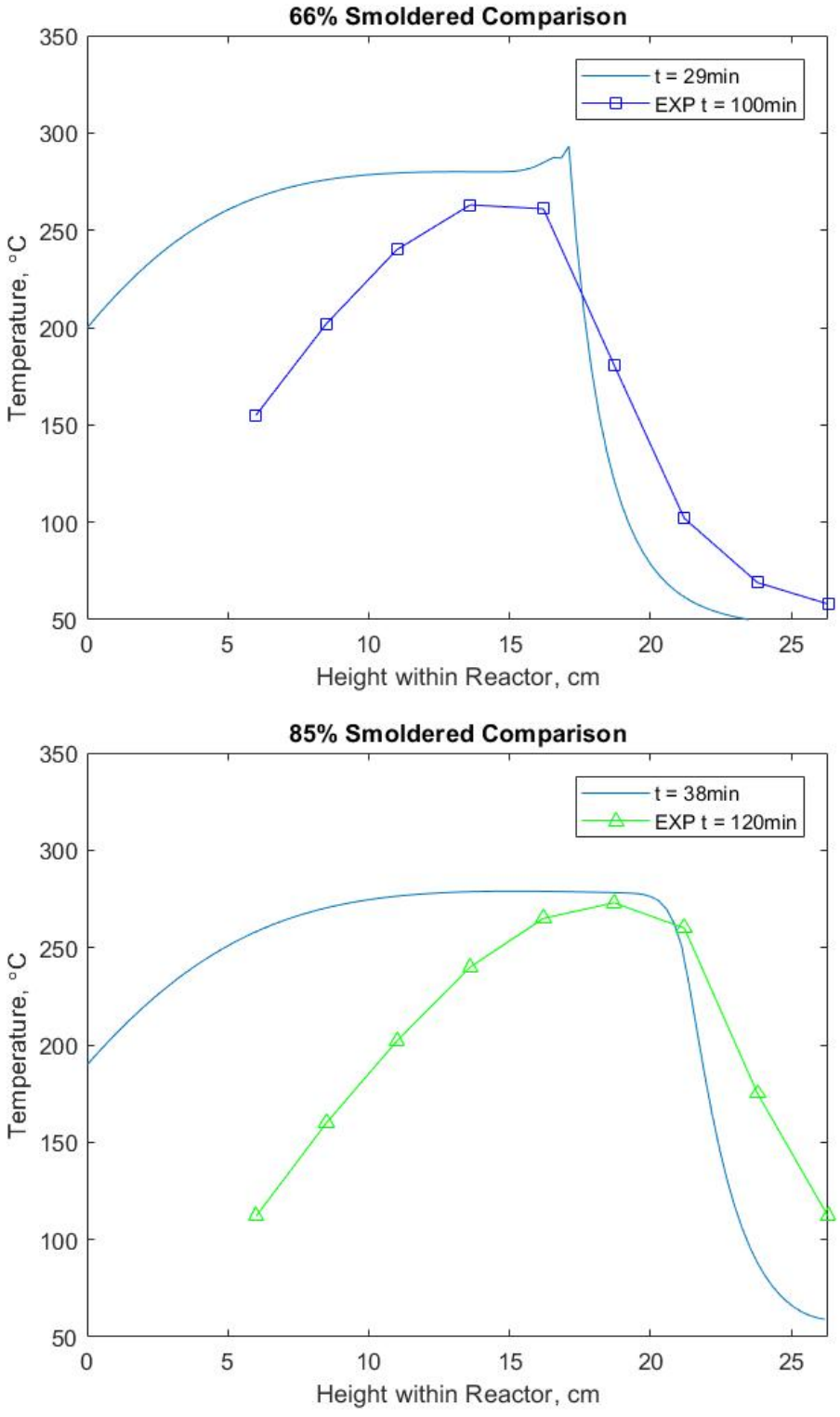

Figure 4.4: Comparison of the temperature profiles at 66% and 85% smoldering completion.

As shown in Figures 4.3 and 4.4, the model seems to consistently predict a steeper temperature decay within the pyrolysis and preheating zones, as well as a higher temperature plateau for the reaction zone. Because the heat generation term was programmed to apply after the ignition temperature of $250°C$ was reached, it is not surprising that the model shows a more abrupt temperature drop between the reaction and pyrolysis zones, where as the experimental values maintain a more gradual transition. This may be remedied by implementing the heat generation term as a ramp instead of a step input, such that not all of the heat energy produced from the smoldering of one node is released at once and in one location. That being said, the differences are not drastic enough to suggest that the original approach is entirely wrong. Since the backwards difference method does take the current surrounding nodal temperatures into account, the approximations still depict a comparable overall trend and allow for visualization of the major heating zones. In the interest of increasing accuracy, however, a program addition that allows the generated nodal heat to diffuse more into its surrounding nodes may decrease the rate of temperature decay, as well as reduce the plateau amplitude.

Recovered Heat Energy	
Average energy recovered:	164 J/g of sand
Average power produced:	733 W per batch
Average Net Power Produced:	333 W per batch

Table 4.1: Results for batch process energy recovery approximations.

As discussed in Chapter 3, the recovered heat energy was calculated using property values associated with the procedure followed to collect the experimental values. The model assumes that 268 g of treated sand, which corresponds to the experimental mass for a 6.4 cm height drop in the waste column, is used to heat 1 kg of room temperature

water at $25°C$. Using the batch average temperature of the first thermocouple located 6.4 cm from the column base, the specific recovered thermal energy was calculated. In comparison to the experimental value of 61 J/g of sand, the model prediction of 164 J/g is optimistic by over 200%. Again, much of this discrepancy stems from the overestimation of the reaction plateau temperature, which extends further back in the model than in reality. For the sake of comparison with the power production values of the gasification-powered competitor, the specific recovered energy was also converted to power produced on a batch scale, which factored in energy consumption of the heaters. Note that this value was calculated assuming that the water and sand mixture took 1 minute to reach the equilibrium temperature. Even considering the gross overestimation, the smoldering model still suggests a net power output in terms of hundreds of watts versus the Cranfield model, which predicts a net output of 2-6 W [6]. Part of this may be attributed to the lack of conversion between thermal and electrical energy, which is present in the Stirling engine used in the Cranfield model.

Although the results for this particular Fourier number and mesh size show promising resemblance to the experimental values, the nature of a finite difference approximation requires that the model must converge to its true solution as the nodal mesh is refined. This follows the logic that the smaller the element size, the more information regarding elemental heat transfer interactions can be captured, which should in turn produce results of greater accuracy and validity. Chapter 5 provides a detailed explanation and analysis of the methods used to evaluate the quality of this model.

Chapter 5

VALIDATION OF THE FINITE DIFFERENCE MODEL

Considering the finite-difference method offers a numerical approximation to problems described by partial differential equations, the accuracy of this estimation must be validated for each case in which it is applied. For the wastewater smoldering experiment, initial generalizations were made in an attempt to describe the observed phenomena in a simplified manner such that the existence and uniqueness of solutions were ensured, based on physically reasonable assumptions. Once a proper problem was constructed, the governing equations were screened for consistency and convergence. The final result included a convergence study to confirm that the approximations approached a true solution for the differential equations as the mesh was refined. The concepts and methods used in this thesis to evaluate stability and convergence were referenced from the second edition of *Difference Methods for Initial-Value Problems* by Richtmyer and Morton [19].

5.1 Model Interpretation for Convergence

To verify model convergence, initial assumptions were made to adequately describe the smoldering experiment with a properly posed initial-value problem, for which the temperature profile at any time, $t > 0$, can be calculated based on an initial temperature profile at $t = 0$. By visualizing the problem in terms of a Banach space, which is defined thoroughly in chapter 2.2 of Richtmyer and Morton [19], the waste column can be represented as a linear vector space, $\mathscr{B}$. To evaluate the temperature distributions for each time step, a one-parameter family $T(t)$ comprised of elements

of $\mathscr{B}$ is desired such that

$$\frac{d}{dt}T(t) = AT(t), \quad 0 \leq t \leq t_{tot} \quad \text{and} \quad T(0) = T_0 \tag{5.1}$$

which can be approximated by the genuine solution,

$$\left\| \frac{T(t+\Delta t) - T(t)}{\Delta t} - AT(t) \right\| \to 0, \quad \text{as } \Delta t \to 0, \quad 0 \leq t \leq t_{tot} \tag{5.2}$$

where A is a linear operator and T_0 is an element of $\mathscr{B}$ representing the assumed initial temperature profile. For qualification as a properly posed problem, two conditions must be met: A unique $T(t)$ must exist for each element, T_0, within $\mathscr{B}$, and the solution $T(t)$ must depend continuously on the initial data, T_0.

In the designated space, $\mathscr{B}$, the finite-difference equations look as follows:

$$B_1 T^{p+1} = B_0 T^p$$

where the linear finite-difference operators $B_0 = B_0(\Delta t, \Delta x_1, \Delta x_2, ...)$ and $B_1 = B_1(\Delta t, \Delta x_1, \Delta x_2, ...)$ are assumed to be independent of parameter t, and dependent on the time step Δt. From here it is assumed that unique function values T^{p+1} are continuously dependent on and can be calculated from any T^p. In addition, it is assumed that B_1^{-1} exists and $B_1^{-1}B_0$ represents a bounded linear transformation within $\mathscr{B}$. When evaluating for stability and convergence, the increasing refinement of the mesh can consist of an infinite sequence of calculations. The main objective, however, is to observe for convergence as Δt and Δx go to zero. For the sake of simplification, Δx may, therefore, be assigned the following relation to Δt, such that $\Delta x \to 0$ as $\Delta t \to 0$:

$$\Delta x_i = g_i(\Delta t), \quad i = 1, 2, ..., d$$

where g represents the space dimension that defines the rate at which $\Delta x \to 0$ with respect to Δt, and d represents the number of g values tested as the mesh becomes refined. Previously introduced in Chapter 3, the existing Fourier correlation,

$Fo = \frac{\alpha \Delta t}{(\Delta x)^2}$, may then be rearranged to comply with this form:

$$\Delta x = \sqrt{\frac{\alpha \Delta t}{Fo}} \tag{5.3}$$

By supposing that the Fo is a positive constant defined by the user for each test during implementation, the linear operators B_1^{-1} and B_0 then become functions of Δt alone and can be written as

$$B_1^{-1}(\Delta t, g_1 \Delta t, g_2 \Delta t, ...) B_0(\Delta t, g_1 \Delta t, g_2 \Delta t, ...) = C(\Delta t),$$

and the finite-difference equation becomes

$$T^{p+1} = B_1^{-1} B_0 T^p = C(\Delta t) T^p. \tag{5.4}$$

Given that finite-difference approximates the time derivative as

$$\frac{d}{dt} T(t) \approx \frac{T^{p+1} - T^p}{\Delta t},$$

from (5.1), it follows that

$$AT(t) \approx \frac{T^{p+1} - T^p}{\Delta t} = \frac{C(\Delta t) T(t) - T(t)}{\Delta t}$$

which, when combined with (5.2), reveals the *Consistency Condition*:

$$\left\| \frac{T(t + \Delta t) - C(\Delta t) T(t)}{\Delta t} \right\| \to 0, \quad \text{as } \Delta t \to 0, \quad 0 \leq t \leq t_{tot} \tag{5.5}$$

where the quantity under the norm constitutes the truncation error, a key component in determining the accuracy associated with any finite-difference model.

5.2 Evaluating Model Accuracy

The accuracy validation of a finite-difference model revolves around three major conditions: Consistency, stability, and convergence. A model exhibits consistency if the truncation error terms tend to zero as the mesh is refined. The stability of a model

imposes a limit on the amplification of any component within the initial function during numerical computation. Convergence indicates that a model approaches the true solution to the problem's differential equations as mesh refinement increases. The Lax Equivalence Theorem states that, for a properly posed initial-value problem with a corresponding finite-difference approximation satisfying the consistency condition, stability is necessary and sufficient for convergence [19]. The validation of these three conditions was performed for all three smoldering case particular differential equations (3.10) to (3.14). The following examples are shown for Case 2 (3.12) for an internal node.

5.2.1 Consistency

The condition stated by (5.5) requires that, for a finite-difference model to provide a consistent approximation to the initial-value problem, the truncation errors must drop out as $\Delta x, \Delta t \to 0$. Truncation errors signify the error that occurs as a result of reducing the differential equations down to finite linear elemental approximations:

$$\begin{aligned}
\frac{\partial}{\partial x} &\approx \frac{1}{\Delta x} \\
\left.\frac{\partial T}{\partial t}\right|_{m} &\approx \frac{T_m^{p+1} - T_m^{p}}{\Delta t} \\
\left.\frac{\partial T}{\partial x}\right|_{m+1,m} &\approx \frac{T_{m+1}^{p+1} - T_m^{p+1}}{\Delta x} \qquad \text{(evaluated at t = p+1)}
\end{aligned}$$

To solve for the truncation error of a differential equation, Case 2 in this example, suppose $\tilde{T}(x,t)$ is an exact solution for (3.12) such that,

$$\rho c\left(\frac{\partial \tilde{T}}{\partial t}\right) = -k\frac{\partial}{\partial x}\left(\left.\frac{\partial \tilde{T}}{\partial x}\right|_{m,m-1} + \left.\frac{\partial \tilde{T}}{\partial x}\right|_{m,m+1}\right) + Q'$$

for which the implicit finite-difference approximations can be substituted, yielding

$$\rho c\left(\frac{\tilde{T}_m^{p+1} - \tilde{T}_m^{p}}{\Delta t}\right) = \frac{-k}{\Delta x}\left(\frac{\tilde{T}_m^{p+1} - \tilde{T}_{m-1}^{p+1}}{\Delta x} + \frac{\tilde{T}_m^{p+1} - \tilde{T}_{m+1}^{p+1}}{\Delta x}\right) + Q'$$

$$\rho c\left(\frac{\tilde{T}_m^{p+1} - \tilde{T}_m^{p}}{\Delta t}\right) - k\left(\frac{\tilde{T}_{m+1}^{p+1} - 2\tilde{T}_m^{p+1} + \tilde{T}_{m-1}^{p+1}}{(\Delta x)^2}\right) - Q' = 0 \qquad (5.6)$$

Using the Taylor series expansion, the differential approximations for the nodal values are as follows:

$$\tilde{T}_m^{p+1} = \tilde{T}_m^p + \Delta t\left(\frac{\partial \tilde{T}}{\partial t}\right)_m^p + \frac{(\Delta t)^2}{2}\left(\frac{\partial^2 \tilde{T}}{\partial t^2}\right)_m^{p+1}$$

$$\tilde{T}_{m+1}^{p+1} = \tilde{T}_m^{p+1} + \Delta x\left(\frac{\partial \tilde{T}}{\partial x}\right)_m^{p+1} + \frac{(\Delta x)^2}{2}\left(\frac{\partial^2 \tilde{T}}{\partial x^2}\right)_m^{p+1} + \frac{(\Delta x)^3}{6}\left(\frac{\partial^3 \tilde{T}}{\partial x^3}\right)_m^{p+1} + \frac{(\Delta x)^4}{24}\left(\frac{\partial^4 \tilde{T}}{\partial x^4}\right)_{m+1}^{p+1}$$

for which continuous partial derivatives are assumed to exist for all applicable orders. Plugging these values into (5.6) results in the following:

$$\rho c\left(\frac{\tilde{T}_m^{p+1} - \tilde{T}_m^p}{\Delta t}\right) - k\left(\frac{\tilde{T}_{m+1}^{p+1} - 2\tilde{T}_m^{p+1} + \tilde{T}_{m-1}^{p+1}}{(\Delta x)^2}\right) = \frac{\rho c \Delta t}{2}\left(\frac{\partial^2 \tilde{T}}{\partial t^2}\right)_m^{p+1} - k\left[\frac{(\Delta x)^2}{2}\left(\frac{\partial^2 \tilde{T}}{\partial x^2}\right)_m^{p+1} - \frac{(\Delta x)^2}{2}\left(\frac{\partial^2 \tilde{T}}{\partial x^2}\right)_m^{p} + \frac{(\Delta x)^4}{24}\left(\frac{\partial^4 \tilde{T}}{\partial x^4}\right)_{m+1}^{p+1} + \frac{(\Delta x)^4}{24}\left(\frac{\partial^4 \tilde{T}}{\partial x^4}\right)_{m-1}^{p+1}\right] \quad (5.7)$$

for which the left-hand side represents the truncation error, for the difference system of Case 2. To verify the consistency of the left-hand side of (5.7), the limit of right-hand side is evaluated as $\Delta x, \Delta t \to 0$, to signify mesh refinement.

$$\lim_{\Delta x \to 0} (5.7),\ \text{RHS} = O(\Delta t)$$

$$\lim_{\Delta t \to 0} (5.7),\ \text{RHS} = O[(\Delta x)^2]$$

$$\lim_{\Delta x, \Delta t \to 0} (5.7) = e[T] = O(\Delta t) + O[(\Delta x)^2]$$

Due to the Fourier correlation assigned earlier in section 5.1, $\Delta x \to 0$ as $\Delta t \to 0$,

$$\therefore \quad e[T] \to 0 \text{ as } \Delta t \to 0,$$

which satisfies the consistency condition for Case 2.

5.2.2 Stability and Convergence

Because the implicit method was used with the goal of minimizing time step constraints, the backwards difference computation of the model is inherently and unconditionally stable. This is a well-known characteristic of implicit difference equations. Consequently, performing the mathematical proof for this behavior was unnecessary for this study. Further information, however, can be found in the reference text [19].

Having isolated and described the smoldering experiment temperature distribution with a properly posed initial-value problem and confirmed its consistency and stability, the Lax Equivalence Theorem may be applied. It is, therefore, implied that the differential solutions are expected to converge to the true solution as the mesh refinement increases for the following convergence study.

5.3 Convergence Study Results

For any finite-difference convergence study, the objective is to observe the different solutions converge to a single true solution as the mesh size decreases incrementally until solution variance becomes negligible. Due to the size of the graphs, the visual results of the convergence study are gathered in Appendix A.

By initially assuming Δx to be related to Δt in terms of the Fourier number, Fo, the increments for mesh refinement can also be controlled in terms of the Fo. Recalling that,

$$Fo = \frac{\alpha \Delta t}{(\Delta x)^2} \quad \Rightarrow \quad \Delta x = \sqrt{\frac{\alpha \Delta t}{Fo}} \qquad \text{and} \qquad \Delta t = \frac{t_{tot}}{p}$$

it follows that as $p \to \infty$, $\Delta t \to 0$, as does Δx. The mesh size, Δx, however, is on the order of $\sqrt{\Delta t}$ and, therefore, decays at a much slower rate than the time step. As the value of Fo increases, so too does the rate at which the mesh size decreases. The process for mesh refinement, therefore, began with increasing the assigned Fo to

increase the rate of refinement. For each Fo value tested, p was increased to observe any trends as the time step, and by relation the mesh size, tended to zero. The convergence study for this model tested a variety of mesh refinements corresponding to the range $0.5 \leq Fo \leq 100$, for which the numerical boundaries were chosen based on computation time, trial-and-error, and the unconditional stability of the implicit method. The average smoldering reaction temperature was chosen as the parameter used to observed convergence since the changing mesh size had the greatest impact on this value relative to other aspects of the temperature profiles.

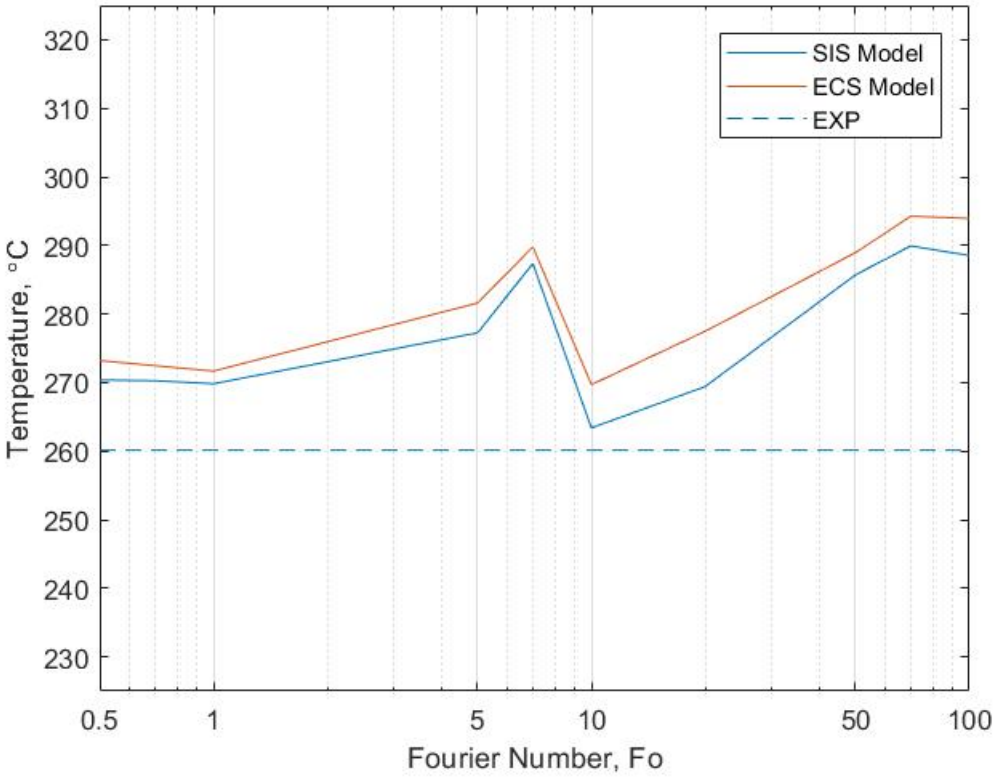

Figure 5.1: Results of convergence study showing the trend in average smoldering reaction temperature.

Figure 5.1 graphs the trend in the average smoldering reaction temperature, which was explained in Chapter 4 as the average post-ignition temperature of the reactor

for each batch smoldering process. Although all values remain within a 50 degree range of the experimental value, increasing the mesh refinement, ultimately, did not display convergence toward a final solution. Instead, a steady decline towards the experimental value is observed for Fo values from 0.5 to 1 before beginning to increase gradually until Fo = 5, after which a peak and a trough occurs at Fo = 7 and 10. This pattern seems to continue in a more expanded form between 10 and 100. This presents a troubling signal for this model since convergence is expected to confirm model validity. Unfortunately, the lack of convergence prevents this model from being trusted to produce accurate results.

Convergence Study		
Fo	p_{max}	$\bar{T}_{reaction}$
0.5	62	270.37
0.7	85	270.27
1	119	269.83
5	230	277.25
7	203	287.35
10	1315	263.38
20	2294	269.41
50	5294	285.71
70	7275	289.93
100	11120	288.53
Average $\bar{T}_{reaction}$:		277.20

Table 5.1: Convergence study results showing the Fourier numbers tested and the corresponding mesh size, p_{max}, and average reaction temperature.

One other notable observation from this study included the existence of a maximum p for each Fo, where, if surpassed, the solution would show that the smoldering

front would die out before all of the fuel in the column had been consumed. As a result, the mesh refinement for each Fo becomes limited by this value, such that a further reduction in the mesh size requires an increase of Fo. This behavior is most likely caused by the method of implementation for the heat generation term, Q', previously explained in Chapter 3. Recalling that,

$$Q' = \frac{H_c \dot{m}}{A_c \Delta x}$$

the heat generation per unit volume contributes the following temperature term to the difference equations:

$$T' = \frac{Q' \Delta t}{\rho c} = \left[\frac{H_c \dot{m}}{\rho c A_c}\right] \frac{\Delta t}{\Delta x} = \mathbb{K} \frac{\Delta t}{\Delta x}$$

where $\mathbb{K}$ represents a positive constant comprised of the constant properties of the fuel and experimental setup. By plugging in (dx eq) for Δx, the above equation becomes,

$$T' = \mathbb{K} \sqrt{\frac{Fo \Delta t}{\alpha}}$$

from which it becomes easy to see that as $p \to \infty$ and $\Delta t \to 0$, $T' \to 0$, rendering the combustion heat generation term negligible. To compromise for this behavior and maintain the pattern of self-sustained smoldering through the entire column, the Fo must be chosen such that it is high enough to ensure that T' does not go to zero before the mesh is sufficiently refined.

Having learned that these approximations do not meet the requirements for consideration as a valid model, the behavior of the temperature distribution over time may not be predicted for this configuration with confidence. That is not to say, however, that this approach should be negated altogether. It is important to acknowledge that, as a pioneering effort to further the study of waste treatment via smoldering combustion, additional research involving both theoretical and experimental validation is necessary before a reliable modeling method can be recommended to assist others in their research endeavors.

Chapter 6

FUTURE DEVELOPMENT AND CONCLUSIONS

This chapter highlights the main learning outcomes from this project. The model that was developed has many limitations, however, various application advantages and opportunities for future development still exist if significant improvements were to be achieved. The following, therefore, outlines the current imperfections and the necessary corrections that should be made to progress towards greater model performance and useful application.

6.1 Limitations

It is yet to be fully understood what aspects cause the lack of model convergence. This, however, represents the main limitation of this modeling method. Although the best results feature numerous visual and numerical similarities to the experimental data, the oscillating trend that begins to appear as the mesh refinement increases suggests that the results cannot be trusted on their own. Typically, a finite difference model converges to the true theoretical solution, at which point a judgment call can be made as to what minimum mesh size is appropriate for approximating a valid solution. Without convergence, however, there is no telling how the trend will continue to fluctuate with mesh refinement. In the context of future studies, this particular model may be able to produce a reasonable simulation of existing experimental results, but, for a fuel type with no existing empirical data, there is no way to predict the thermal behavior with any practical degree of certainty.

One aspect to note is that the convergence was evaluated based solely on the average reaction temperature, $\bar{T}_{reaction}$, which may not have been the the best param-

eter to use for validation. $\bar{T}_{reaction}$ was calculated as a representative value for the smoldering combustion temperature throughout the overall batch reaction, since this value changed the most with respect to mesh refinement. Other parameters, such as the rate of temperature decay in the pyrolysis zone, remained rather consistent by comparison. Because $\bar{T}_{reaction}$ is an average of averages, however, it does not by any means offer an inherently accurate value. It would, therefore, be useful to further explore how to quantify model convergence in terms of which parameters convey key information.

Looking closer at the internal logic within the model, the mesh-dependent generation term, T', presents a key factor that most likely instigates to the lack of convergence. As was touched on in Chapters 4 and 5, the implementation of the heat generation term occurs as a step input following a conditional statement. Because the model is expected to generate heat for any node that has reached a temperature between 250 and 280$°C$, as shown in Figure 3.10, this presents a 30 degree range in which any qualifying node is modeled to release the entirety of its heat generation capacity. In addition, the generation term only has a direct effect on the node from which it is released. The adjacent nodes only feel its affect due to the increased temperature of the current node, which gets factored into the simultaneous finite-difference calculation. Perhaps if this input was modeled to diffuse more across adjacent nodes, temperature spikes, such as the one seen at the smoldering front in the top half of Figure 4.4, would be reduced or eliminated. This in turn may encourage the $\bar{T}_{reaction}$ value to converge, since it is calculated as the average of all temperatures above 245$°C$.

As mentioned towards the end of Chapter 5, T', is also proportional to the time step, Δt, as well as the rate of fuel mass destruction, $\dot{m}$. Because the $\dot{m}$ was implemented as a constant pulled from the experimental data, the affects of fluctuating this value were not studied in this thesis. That being said, the $\dot{m}$ value used in this

model may not accurately reflect the proper destruction rate based on the rest of the parameters. Discussion on methods for remedying this issue continues in Section 6.3.

Should corrections to the heat generation implementation lead to model convergence, this study could offer a useful baseline for better understanding the thermal behavior associated with smoldering for residential waste treatment. As the driving force behind the model's self-sustainability, all other issues will be affected by any changes to this process. It would, therefore, be necessary to completely re-evaluate the model's limitations following any alterations to the heat generation term.

6.2 Advantages

As a parameter based model, the ability to predict the temperature behavior of various fuel types makes this a useful tool for pioneering research. Assuming that the limitations explained above can be overcome, an accurate model would offer a convenient alternative to running physical experiments. The expenses associated with gathering empirical data add up when accounting for raw materials, time and labor. Although physical confirmation is eventually necessary, a functioning smoldering model could provide a more efficient method for establishing a starting point for researching various fuel feeds. Ideally, the model may be used for three speculative approaches: parameter-based behavior, behavior-based parameters, and fuel feed research refinement.

Using the known physical and thermal property values of the fuel matrix, researchers may generate hypothetical temperature profiles. This approach describes the process used to develop the model. It may also be used in a backwards fashion to, then, suppose property values for an unknown fuel matrix if given the temperature data. Although the property values of the fuel matrix in E6 were calculated or assumed using the original experiment descriptions, the precise properties for a fuel

matrix of 33% moisture content with a 24:1 sand to fuel ratio remain unidentified. Beginning with these initial property values, an ideal model would allow the user to tweak each parameter and observe the resulting temperature profiles to determine more accurate values. A trustworthy model would also enable researchers to narrow down corresponding fuel property values for achieving desired temperature profiles. Those values may then be used to select a more promising set of fuels for experimental trials, as opposed to choosing a lineup without the being able to speculate the outcomes.

The ability to obtain theoretical smoldering data would save time and money, which, in a research setting, are highly limited resources. Although the current approximations are far from offering the capabilities of an ideal model, the possible benefits of improving its approach prompt the question of what must be done to develop this technology in the future.

6.3 Future Development

Having only recently emerged as a viable waste treatment option, smoldering combustion is still a long way from being well understood to the point of practical efficiency. Even with this model being the first to tackle off-grid residential scale sewage smoldering, the batch combustion that it simulates still represents an archaic process. While batch smoldering remains consistently effective in properly treating and reducing waste volume, continuous smoldering seems to be the method of interest, regarding the University of Toronto prototype. This technique, which features a stationary smoldering front with a moving fuel matrix, has been shown to increase smoldering velocity and specific recoverable heat energy [3]. In addition, the constant movement of the fuel matrix hypothetically eliminates the need for a full-sized waste column, making for a more compact system. The prototype logistics between this theoretical

system and the manually run batch experiments, however, have yet to be determined. Given that both the model and experiments only consider the smoldering reactor outside of the entire appliance, connections must still be made to factor in the systems required for fuel loading and unloading. In addition to the cartridge heaters, the mechanical energy necessary to prepare and deposit the fuel will affect the system's capacity for self-sustainability. As of this publication, a functioning prototype has not been built and detail designs have not been released.

Other factors to further research are the time and destruction rate dependency of the temperature generation term, T'. A better implementation would include $\dot{m}$ as a function based on the smoldering front progression. In addition, the maximum p-value for each Fo number seen during the convergence studies suggests an error in the heat generation term with respect to the time step, Δt. It would, therefore, be worthwhile to further study the experimental affects of T' overtime, perhaps with more detailed data collection methods. In general, the specific data set around which this model was constructed featured limitations of its own. Now knowing the results of this model and how it may be improved, a more comprehensive experimental data acquisition setup may be suggested. Gaining access to empirical temperature profiles with more thermocouples and smaller time steps would offer much more information regarding boundary heat losses and for visualizing the affects of the heat generation term.

6.4 Conclusions

From the beginning of this project, the desired outcome was to develop a simplified model for smoldering combustion specific to residential sewage treatment. Since the complexity of existing smoldering models can present difficult and possibly unnecessary obstacles the mathematical characterization and simulation of sewage smoldering

combustion became the main objective. As a wastewater treatment method, smoldering combustion has shown much promise in an experimental setting. Because this technology has only recently been explored for this application, a formal understanding of the phenomena can take time and several trials to develop. It is, therefore, useful to begin with the most simple approach to the problem, even if the method ultimately becomes irrelevant. As a result, the experimental configuration was reduced to a highly-simplified form using basic assumptions. It was expected that this approach would yield over-simplified results, however, collecting this information would still provide a baseline for comparison with the published experimental data.

The project was developed around the parameters associated with a specific prototype system design, hoping to establish a framework, such that the parameters could eventually be altered for different configurations. The smoldering reactor was modeled as a one-dimensional, homogeneous, solid control volume with specialized boundary conditions, from which the governing heat equations were derived. The transient nature of the experimental results led to the use of finite-difference methods, such that, for a given time step, the temperatures at each node were calculated simultaneously using system of equation matrices. The initial temperature profile at time $t = 0$ was simulated using a cylindrical extended fin model and provided the computational foundation for the resulting temperature profiles. The heat generated due to smoldering was implemented as a step input using three logical combustion conditions. The derived numerical computation equations were solved using a program written in Matlab. The resulting graphs were tailored for both model and experimental comparison, as well as visualization of the smoldering front propagation.

In the best-case scenario, an ideal model would have been able to accurately estimate thermal behavior for energy recovery analysis, as well as comparison with other alternatives. Having learned that this model does not meet the requirements

for validity, however, the transient temperature behavior may not be predicted with confidence. That is not to say, however, that this approach should be negated altogether. It is important to acknowledge that, as a pioneering effort to further the study of waste treatment via smoldering combustion, additional research involving both theoretical and experimental validation is necessary before a reliable modeling method can be recommended to assist others in their research endeavors.

Bibliography

[1] Brown and Caldwell. "Gasification of Sludge and Biosolids:A Review of Technology Fundamentals and the Current Commercial Status". In: *PNCWA*. Oct. 2012. URL: www.pncwa.org/assets/2012Conf/Presentations/Session_20_Energy_Recovery/winkler_gasification_sludge_biosolids.pdf.

[2] C. Campbell and M. Ogden. *Constructed Wetlands in the Sustainable Landscape*. New York: Wiley, 1999.

[3] I. Fabris and et al. "Continuous, self-sustaining smouldering destruction of simulated faeces". In: *Fuel* 190 (Feb. 2017), pp. 58–66.

[4] *Gasification vs. Combustion*. Procone GmbH GAsification Systems. 2018. URL: procone.org/gasification-vs.-combustion.html.

[5] Nicholas Gray. *Biology of Wastewater Treatment*. 2nd ed. Print. Imperial College Press, 2004.

[6] D. Hanaka and et al. "Conceptual energy and water recovery system for self-sustained nano membrane toilet". In: *Energy Conversion and Management* 126 (Oct. 2016), pp. 352–361.

[7] *How Much Does A Septic System Cost?* Home Advisor: True Cost Guide. 2018. URL: www.homeadvisor.com/cost/plumbing/install-a-septic-tank/.

[8] *How Much Does It Cost To Install A Sewer Main?* Home Advisor: True Cost Guide. 2018. URL: www.homeadvisor.com/cost/plumbing/install-a-sewer-main/.

[9] Incinolet. Incinolet Electric Incinerating Toilet. 2017. URL: incinolet.com/.

[10] F. Incropera and D. DeWitt. *Fundamentals of Heat and Mass Transfer*. 7th ed. Print. New York: J. Wiley, 2002.

[11] *Knowledge Hub*. SUSANA Sanitation Portal. 2018. URL: www.susana.org/en/knowledge-hub.

[12] J. Metz, A. Floyd, and M. Boerman. *2016 Water Resources Status Report*. Tech. rep. City of San Luis Obispo, June 2017. URL: www.slocity.org/home/showdocument?id=14623.

[13] A. Mountouris, E. Voutsas, and D. Tassios. "Plasma gasification of sewage sludge: Process development and energy optimization". In: *Energy Conversion and Management* 49.8 (2008), pp. 2264–2271.

[14] *Nature's Head Composting Toilet*. 2018. URL: natureshead.net.

[15] T. J. Ohlemiller. "Modeling of Smoldering Combustion Propagation". In: *Fire Research and Safety* 639 (Sept. 1982). Center for Fire Research, National Bureau of Standards, pp. 266–307.

[16] *Onsite Wastewater Treatment System Repair of Failure/Malfunction Survey*. Tech. rep. California Wastewater Training & Research Center, California State University, Chico, Jan. 2003. URL: www.waterboards.ca.gov/water_issues/programs/owts/docs/onsite_repairsrpt2003.pdf.

[17] *Reinventing the Toilet*. University of Toronto, Faculty of Applied Sciences & Engineering. 2018. URL: cgen.utoronto.ca/research-initiatives/current-projects/re-invent-the-toilet-challenge/.

[18] *Review of Technologies for Gasification of Biomass and Wastes*. Tech. rep. DECC and NNFCC, June 2009. URL: wiki.gekgasifier.com/f/Review+of+Biomass+Gasification+Technologies.NNFCC.Jun09.pdf.

[19] K. Richtmyer R. & Morton. *Difference Methods for Initial-Value Problems*. 2nd ed. Interscience tracts in pure and applied mathematics ; no. 4. Print. New York: Interscience, 1967.

[20] A. Rostami, J. Murthy, and M. Hajaligol. "Modeling of a smoldering cigarette". In: *Journal of Analytical and Applied Pyrolysis* 66 (Jan. 2003), pp. 281–301.

[21] *Sewer Connection Cost*. Cost Helper: Home and Garden. 2018. URL: home.costhelper.com/sewer-connection.html.

[22] *Sewer Lateral Connections and Septic System Decommissioning*. Public Works, County of San Luis Obispo. 2017. URL: www.slocounty.ca.gov/Departments/Public-Works/Current-Public-Works-Projects/Los-Osos-Wastewater-Project/Sewer-Lateral-Connections-and-Septic-System-Decomm.aspx.

[23] *Sewer Main Installation Price*. ImproveNet. 2018. URL: www.improvenet.com/r/costs-and-prices/sewer-installation-cost-guide.

[24] A. Siirala. *Comparison of gasification, pyrolysis and combustion*. Tech. rep. AALTO University School of Chemical Technology, Nov. 2013. URL: advancedbiofuelsusa.info/wp-content/uploads/2010/05/8_gasification_pyrolysis_combustionRevised.pdf.

[25] *The Engineering ToolBox*. Online. 2001. URL: www.engineeringtoolbox.com.

[26] *The Global Syngas Technologies Council, GSTC*. 2018. URL: www.gasification-syngas.org.

[27] *The Nano Membrane Toilet*. Cranfield University. 2018. URL: www.nanomembranetoilet.org.

[28] *Toilets: Frugal Flushing*. Home Water Works. 2017. URL: www.home-water-works.org/indoor-use/toilets.

[29] USEPA. *Case Studies of Individual and Clustered (Decentralized) Wastewater Management Programs*. 2012. URL: www.epa.gov/sites/production/files/2015-06/documents/decentralized-case-studies-2012.pdf.

[30] USEPA. *Constructed Wetlands*. 2017. URL: www.epa.gov/wetlands/constructed-wetlands.

[31] USEPA. *Onsite Wastewater Treatment Systems Manual*. 2002. URL: www.epa.gov/sites/production/files/2015-06/documents/2004_07_07_septics_septic_2002_osdm_all.pdf.

[32] USEPA. *Principles of Design and Operations of Wastewater Treatment Pond Systems for Plant Operators, Engineers, and Managers*. 2011. URL: www.epa.gov/sites/production/files/2014-09/documents/lagoon-pond-treatment-2011.pdf.

[33] USEPA. *Types of Anaerobic Digesters*. 2016. URL: www.epa.gov/anaerobic-digestion/types-anaerobic-digesters.

[34] USEPA. *Why Maintain Your Septic System*. 2017. URL: www.epa.gov/septic/why-maintain-your-septic-system.

[35] M. Vaughan. *Los Osos homeowners could be fined $5,500 a day for failing to connect to sewer*. The Tribune. May 2017. URL: www.sanluisobispo.com/news/local/article148522254.html.

[36] *What is a septic system? How do I maintain one?* National Environmental Services Center (NESC). West Virginia University. 2016. URL: www.nesc.wvu.edu/subpages/septic_defined.cfm.

[37] *What Kind Of Septic System Is Best For Me? Dutchess County, NY Septic Tank Installation*. Home Insider. 2016. URL: homeinsider.org/what-kind-of-septic-system-is-best-for-me-dutchess-county-ny-septic-tank-installation/.

[38] World Health Organization (WHO). *The United Nations World Water Development Report 2017: Facts and Figures*. Tech. rep. UNESCO, 2017. URL: unesdoc.unesco.org/images/0024/002475/247553e.pdf.

[39] World Health Organization (WHO). *The United Nations World Water Development Report 2017: Wastewater the Untapped Resource*. Tech. rep. UNESCO, 2017. URL: unesdoc.unesco.org/images/0024/002471/247153e.pdf.

[40] L. Yerman and et al. "Self-sustaining Smouldering Combustion as a Waste Treatment Process". In: *Intech* (2016), pp. 143–166.

[41] L. Yerman and et al. "Smouldering combustion as a treatment technology for faeces: Exploring the parameter space". In: *Fuel* 147 (May 2015), pp. 108–116.

APPENDICES

Appendix A

MATLAB MODEL CODE

The following displays the published MATLAB code for the model used to generate the results for this thesis.

```
%==========================================================================================
%%                  SMOLDERING COMBUSTION FINITE-DIFFERENCE MODELING
%==========================================================================================
% Laura Kawashiri
% Master's Thesis

clc
close all
clear all

% Note: For indexing purposes, it must be taken into account that Matlab arrays begin
% with 1 instead of 0 and the array convention is A(rows,columns).

%------------------------------------------------------------------------------------------
% DEFINING PROPERTIES
%------------------------------------------------------------------------------------------
% Because sand constitutes the majority of mass within the porous matrix, we assume
% that the heat transfer within the waste column can be evaluated using the
% properties of sand alone.

rho = 2.122;                %[g/cm^3]           porous matrix density
c_s = 0.83;                  %[J/g*degC]         heat capacity of sand
    thermCond = 2;          %[W/m*degC]         thermal conductivity of (moist) sand
K = thermCond*3600*.01;     %[J/h*cm*degC]      ^(unit conversion)
a = K/(rho*c_s);            %[cm^2/h]           alpha term for simplifying heat eqns.
    cc_b = 20;              %[W/m^2*degC]       convection coeff. @ base
h_b = cc_b*(10^-4)*3600;    %[J/h*cm^2*degC]    ^(unit conversion)
    cc_t = 10;              %[W/m^2*degC]       convection coeff. @ top (free)
h_t = cc_t*(10^-4)*3600;    %[J/h*cm^2*degC]    ^(unit conversion)
e = 1;                      %[]                 emissivity (assume 1 for blackbody)
s = 5.67*(10^-12)*3600;     %[J/h*cm^2*degC^4]  Boltzmann constant

%------------------------------------------------------------------------------------------
% FUNCTION VARIABLE INCREMENTATION
%------------------------------------------------------------------------------------------
% Since the temperature along the waste column is a function of two
% variables, position and time, T(t,x), we establish incrementation for both to
% perform finite-difference analysis. For the sake of consistency, let dx(dt).

t_tot = 2;                  %[h]            duration of simulation
p = 230;                     %[]             number of time increments
dt = t_tot/(p-1);           %[h]            timestep value
Fo = 5;                     %[]             Fourier number
L = 26.3;                   %[cm]           total length of waste column
dx = sqrt(a*dt/Fo);         %[cm]           position step value
m = round((L/dx)+1);        %[]             number of x-position increments
Bi_b = (h_b*dx)/K;          %[]             Biot number @ base
Bi_t = (h_t*dx)/K;          %[]             Biot number @ top
```

```
%-------------------------------------------------------------------------------
% HEAT GENERATION CONSTANT
%-------------------------------------------------------------------------------
% At the smoldering front, we assume waste is combusting and generating heat energy.
% This value is calculated using the following properties for waste fuel combustion.

H_c = 20600;                %[J/g]          heat of combustion for dry fuel
m_dot = 27.5;               %[g/h]          dry fuel destruction rate
D = 6.25;                   %[cm]           diameter of waste column
A = (pi()*D^2)/4;           %[cm^2]         cross-sectional area of waste column
Vf = A*dx;                   %[cm^3]         total waste column volume
Q_gen = (H_c*m_dot)/(Vf);       %[J/h*cm^3]     rate of heat energy generation

%-------------------------------------------------------------------------------
% INITIAL TEMPERATURE PROFILE (ITP) + POSITION AND TIME ARRAY SETTINGS
%-------------------------------------------------------------------------------
% An initial temperature profile (ITP) is needed to begin the finite-difference
% study. This equation describes the temperature distribution along the x-axis at
% time t = 0, at which we have assumed the bottom of the waste column has just
% ignited and the smoldering front is at x = 0.

T_ig = 250;                 %[degC]         ignition temperature
T_f = 50;                   %[degC]         initial temperature of virgin fuel
T_sur = 25;                 %[degC]         temperature of ambient air
t_h = 0.25;                 %[h]            time needed to first heat fuel to T_ig
T = zeros(p,m);             %[degC]         set up array for temp. values

% The ITP can be generated using one of two equations. The first models the waste
% column as a semi-infinite solid with a constant surface temperature, given the
% assumptions that the base has ignited at T_ig and the lateral boundary is
% adiabatic. The second model depicts the column as an extended cylindrical fin with
% a base temperature, T_ig, and convective heat transfer at the tip. This option
% requires that a convection term be applied to the lateral boundary.
% Both assume the following conditions:
%           - 1D steady state heat conduction
%           - constant/uniform properties
%           - uniform cross-sectional temperature distribution
%           - no radiation
%           - no heat generation

ITP_type = 1;               %[]             = 1 to use semi-infinite solid eqn.
%                                           = 2 to use extended surface eqn.

for i = 1
    for j = 1:m
        x(i,j) = dx*(j-1);  %[cm]           est. array for x at each increment
%       ------------------------ Semi-Infinite Solid Model -------------------------
        if ITP_type == 1
            T(i,j) = (T_f-T_ig)*erf(x(i,j)/(2*sqrt(a*t_h)))+T_ig;
```

```
                            %[degC]         temp. profile eqn for semi-infinite
%                                           solid w/ const. surface temp. at t=0
%       ------------------------- Extended Surface Model --------------------------
        elseif ITP_type == 2
            h_l = 3.24;
                            %[J/h*cm^2*degC]equivalent convection coeff. to represent
%                                           radial heat loss
            if j == 1
                T(i,j) = T_ig;
            else
                tp_m = sqrt((h_t*4)/(K*D));
                            %[cm^-1]
                w = (cosh(tp_m*(L-x(i,j)))+(h_l/(tp_m*K))*sinh(tp_m*(L-x(i,j)))) ...
                    /(cosh(tp_m*L)+(h_l/(tp_m*K))*sinh(tp_m*L));
                T(i,j) = w*(T_ig-T_f)+T_f;
                            %[degC]         temp. profile eqn for extended
                            %               cylindrical fin w/ convection at the tip
            end
%       ---------------------------------------------------------------------------
        else
            disp('Invalid ITP_type Entry. Choose 1 or 2.');
        end
    end
end
for i = 1:p
    t(i,1) = dt*(i-1);      %[h]            array for time at each increment
end

%---------------------------------------------------------------------------------
% TEMPERATURE EVALUATION USING FINITE-DIFFERENCE
%---------------------------------------------------------------------------------
% The conditional statement that determines which finite-difference method to use is
% based on the stability criterion regarding the Fourier number. For a Fo number
% above 1/2, the explicit method is unstable. Therefore, the implicit method is used
% for the following calculations. This bases the present temperature of a desired
% node on the present temperatures of surrounding nodes, which are calculated
% simultaneously using matrices.

VFmarker = zeros(1,m);  % Virgin fuel indicator for each

M = zeros(m,m);         % est. M matrix of temperature scalars for each timestep
C = zeros(m,1);         % est. C column matrix of previous temp.s for each timestep
for i = 1:p-1                               % for each timestep
    for j = 1:m                             % for each position increment
%-------1st Node Boundary Check-------------------------------------------------------
        if j-1 == 0
            M(j,j) = 1+2*Fo+2*Fo*Bi_b;
            M(j,j+1) = -2*Fo;
%           Ignition Check-----------------------------------------------------------
```

```
            if T(i,j) >= 250 && T(i,j) <= 280
%               VF Check-------------------------------------------------------------
                if VFmarker(1,j)== 0
                    Q_g = Q_gen;
                    VFmarker(1,j) = 1;
                    SFendtime = i;
                else
                    Q_g = 0;
                end
            else
                Q_g = 0;
            end
            C(j,1) = T(i,j)+(2*Fo*Bi_b*T_sur)+((dt*Q_g)/(rho*c_s));
%-------Last Node Boundary Check-----------------------------------------------------
        elseif j+1 > m
            h_r(i) = e*s*(T(i,j)+T_sur)*(T(i,j)^2+T_sur^2);
%                                           % evaluates radiation coeff. @
%                                           % previous timestep
            M(j,j-1) = -2*Fo;
            M(j,j) = 2*Fo+2*Bi_t*Fo+2*Bi_t*Fo*(h_r(i)/h_t)+1;
%           Ignition Check-------------------------------------------------------------
            if T(i,j-1) >= 250 && T(i,j-1) <= 280
%               VF Check-------------------------------------------------------------
                if VFmarker(1,j)== 0
                    Q_g = Q_gen;
                    VFmarker(1,1:j) = 1;
                    SFendtime = i;
                else
                    Q_g = 0;
                end
            else
                Q_g = 0;
            end
            C(j,1) = T(i,j)+(2*Bi_t*Fo*(1+(h_r(i)/h_t))*T_sur)+((dt*Q_g)/(rho*c_s));
%-------Internal Nodes---------------------------------------------------------------
        else
            M(j,j) = 1+2*Fo;                % diagonal values for M
            M(j,j-1) = -Fo;
            M(j,j+1) = -Fo;
%           Ignition Check
            if T(i,j-1) >= 250 && T(i,j-1) <= 280
%               VF Check
                if VFmarker(1,j)== 0
                    Q_g = Q_gen;
                    VFmarker(1,1:j) = 1;
                    SFendtime = i; % marker that will indicate # of timesteps taken↙
to completely smolder waste column
                else
                    Q_g = 0;
```

```
                end
            else
                Q_g = 0;
            end
            C(j,1) = T(i,j)+((dt*Q_g)/(rho*c_s));
        end
    end
    T(i+1,:) = inv(M)*C;    % calculates the current temperature profile as a matrix
end

% For use in the later convergence studies...
Y = zeros(SFendtime,m);
Yavg = zeros(SFendtime,1);
for i = 1:SFendtime
    Y(i,:) = T(i,:).*(T(i,:)>245);
    Yavg(i,1) = mean(Y(i,find(Y(i,:)>245)));
end
Yline = mean(Yavg);
%-------------------------------------------------------------------------------
% ENERGY RECOVERY ESTIMATION
%-------------------------------------------------------------------------------
% Recoverable energy is determined by theoretically heating an arbitrary mass of
% room temp. water with an arbitrary mass of sand from 3.8cm above the base of the
% column. This resembles the procedure used to measure recoverable heat empirically.

m_h2o = 1000;               %[g]
c_h2o = 4.184;              %[J/g*degC]
Ti_h2o = 25;                %[degC]
m_s = 268;                  %[g]
TC1 = 6.4;                  %[cm]
for i = 1:p-1
    Ti_s(i,1) = T(i,round(TC1/dx));
    Tfinal(i,1) = (m_s*c_s*Ti_s(i)+m_h2o*c_h2o*Ti_h2o)/(m_s*c_s+m_h2o*c_h2o);
                            %[degC]
    Q_rec(i,1) = m_h2o*c_h2o*(Tfinal(i)-Ti_h2o)/m_s;
                            %[J/g]          Recovered energy per g of sand
end
Q_recAVG = mean(Q_rec);     %[J/g]          Average recovered energy
disp(['Average energy recovered: ',num2str(Q_recAVG),' J/g of sand']);

Pwr_prod = Q_recAVG*m_s/60;    %[W]            Power produced per cycle by the system
H_pwr = 200;                %[W]            Cartridge heater power delivered (heat)
H_num = 2;                  %[]             Number of heaters
%H_use = 3600;               %[h]            Hours in use per cycle
H_pwr_tot = H_num*H_pwr;
                            %[W]          Total electrical power consumed by heaters
Net_Pwr = (Pwr_prod)-H_pwr_tot;
                            %[W]          Net System Power
```

```
disp(['Average power produced: ',num2str(Pwr_prod),' W per batch']);
disp(['Average Net Power Produced: ',num2str(Net_Pwr),' W per batch']);

%-------------------------------------------------------------------------------------
% PLOTS
%-------------------------------------------------------------------------------------
% Figure 1 graphs the temperature profiles at 4 dispersed points in time and the
% temperature profiles for all timesteps with respect to position along the waste
% column.

% Data for Correlation
x_EXP = [6,8.5,11,13.6,16.2,18.7,21.2,23.8,26.3];
EXP_T80 = [220,250,249,180,100,65,55,53,51];
EXP_T100 = [155,202,240,263,261,181,102,69,58];
EXP_T120 = [112,160,202,240,265,273,260,175,112];

% Main Figure with Comparison and Sustainability Progression
f = figure;
set(gcf, 'Units', 'Normalized', 'OuterPosition', [0, 0.04, 0.75, 0.96]);
img = uipanel('Parent',f,'BorderType','none');
img.Title = ['Temperature Profiles vs. Reactor Height for Fo = ', num2str(Fo),', p =↙
',num2str(p)];
img.TitlePosition = 'centertop';
img.FontSize = 12;
img.FontWeight = 'bold';

subplot(2,1,1,'Parent',img)
plot(x(1,:),T(1,:),x(1,:),T(round(SFendtime*0.47),:), ...
    x(1,:),T(round(SFendtime*0.66),:),x(1,:),T(round(SFendtime*0.85),:))
hold on
plot(x_EXP(1,:),EXP_T80(1,:),'r-o',x_EXP(1,:),EXP_T100(1,:),'b-s',x_EXP(1,:),EXP_T120↙
(1,:),'g-^')
hold off
xlim([0 26.3])
ylim([25 350])
title('Four-Time Profiles')
xlabel('Height within Reactor, cm')
ylabel('Temperature, \circC')
legend ('t = 0', ['t = ' num2str(round(t(round(SFendtime*0.47))*60)) 'min'], ...
    ['t = ' num2str(round(t(round(SFendtime*0.66))*60)) 'min'], ...
    ['t = ' num2str(round(t(round(SFendtime*0.85))*60)) 'min'], ...
    'EXP t = 80min', 'EXP t = 100min', 'EXP t = 120min')
legend ('Location', 'northeastoutside')

subplot(2,1,2,'Parent',img)
for i = 1:round(SFendtime/10):SFendtime+5
    if i <= SFendtime
        plot(x(1,:),T(i,:))
        hold on
```

```
    else
        plot(x(1,:),T(SFendtime+5,:))
        hold on
    end
end
line([0,L],[Yline,Yline],'LineStyle','--')
        hold off
xlim([0 26.3])
ylim([25 350])
title('Smoldering Progression')
xlabel('Height within Reactor, cm')
ylabel('Temperature, \circC')

% Separated Comparisons
figure(2)
plot(x(1,:),T(round(SFendtime*0.47),:))
hold on
plot(x_EXP(1,:),EXP_T80(1,:),'r-o')
hold off
xlim([0 26.3])
ylim([50 350])
title('47% Smoldered Comparison')
xlabel('Height within Reactor, cm')
ylabel('Temperature, \circC')
legend(['t = ' num2str(round(t(round(SFendtime*0.47))*60)) 'min'],'EXP t = 80min')

figure(3)
plot(x(1,:),T(round(SFendtime*0.66),:))
hold on
plot(x_EXP(1,:),EXP_T100(1,:),'b-s')
hold off
xlim([0 26.3])
ylim([50 350])
title('66% Smoldered Comparison')
xlabel('Height within Reactor, cm')
ylabel('Temperature, \circC')
legend(['t = ' num2str(round(t(round(SFendtime*0.66))*60)) 'min'],'EXP t = 100min')

figure(4)
plot(x(1,:),T(round(SFendtime*0.85),:))
hold on
plot(x_EXP(1,:),EXP_T120(1,:),'g-^')
hold off
xlim([0 26.3])
ylim([50 350])
title('85% Smoldered Comparison')
xlabel('Height within Reactor, cm')
ylabel('Temperature, \circC')
legend(['t = ' num2str(round(t(round(SFendtime*0.85))*60)) 'min'],'EXP t = 120min')
```

```
% CONVERGENCE STUDY PLOTS
% Data from Convergence Study
CS_Fo = [0.5,0.7,1,5,7,10,20,50,70,100];
CS_Yline1 = [270.37,270.27,269.83,277.25,287.35,263.38,269.41,285.71,289.93,288.53];
CS_Yline2 = [273.20,272.46,271.67,281.60,289.78,269.70,277.48,288.95,294.26,293.94];
EXP_Yline = 260.1428571;

figure(5)
semilogx(CS_Fo(1,:),CS_Yline1(1,:))
hold on
semilogx(CS_Fo(1,:),CS_Yline2(1,:))
hold on
line([0.5 100],[260.1428571,260.1428571],'LineStyle','--')
hold off
xlim([0.5 100])
ylim([225 325])
xticks([0.5,1,5,10,50,100])
xticklabels({'0.5','1','5','10','50','100'})
xlabel('Fourier Number, Fo')
ylabel('Temperature, \circC')
legend('SIS Model','ECS Model','EXP')
ax = gca;
ax.XGrid = 'on';
```